Doctoral Dissertations   Student Theses and Dissertations

Spring 2016

Cable analysis for electromagnetic compatibility issues

Guanghua Li

Recommended Citation

CABLE ANALYSIS FOR ELECTROMAGNETIC COMPATIBILITY ISSUES

by

GUANGHUA LI

A DISSERTATION

Presented to the Faculty of the Graduate School of the

MISSOURI UNIVERSITY OF SCIENCE AND TECHNOLOGY

In Partial Fulfillment of the Requirements for the Degree

DOCTOR OF PHILOSOPHY

in

ELECTRICAL ENGINEERING

2016

Approved by:

David J. Pommerenke, Advisor
James L. Drewniak
Jun Fan
Victor Khilkevich
Klaus Woelk

PUBLICATION DISSERTATION OPTION

This dissertation consists of the following three papers, formatted in the style used by the Missouri University of Science and Technology, listed as follows:

Paper 1, G. Li, K. Itou, Y. Katou, N. Mukai, D. Pommerenke, and J. Fan, "A resonant E-field probe for RFI measurements," IEEE Trans. EMC, vol. 56, no. 6, pp. 1719-1722, Dec. 2014.

Paper 2, G. Li, W. Qian, A. Radchenko, J. He, T. Van Doren, D. Beetner, D. Pommerenke, G. Hess, and R. Hoeckele, "Prediction of radiated emissions from cables over a metal plane using a SPICE model," IEEE Trans. EMC, vol. 57, no. 1, pp. 61-68, Feb. 2015.

Paper 3, G. Li, G. Hess, R. Hoeckele, P. Jalbert, S. Davidson, V. Khilkevich, T. Van Doren, D. Pommerenke, and D. Beetner, "Measurement-based modeling and worst-case estimation of crosstalk inside an aircraft cable connector," IEEE Trans. EMC, vol. 57, no. 4, pp. 827-835, Aug. 2015.

ABSTRACT

This dissertation consists of three papers. In the first paper, a high-sensitivity resonant electric field probe was designed, consisting of an LC resonator loaded by quarter-wave transformers. At the resonant frequency of 1.577 GHz, the measured $|S_{21}|$ from a matched trace to the resonant probe was approximately 6.6 dB higher than that of an equivalently sized broadband probe.

In the second paper, a method for creating a simple SPICE model is proposed such that the SPICE model allows prediction of radiated emissions in component level tests. The radiation from the ground connections between the cables and return plane dominates over the radiation from the horizontal cables.

In the third paper, a methodology for measuring coupling parameters and modeling crosstalk within aircraft cable connectors at low frequencies (< 400 MHz) was developed. The accuracy of the model was evaluated through comparison of simulated and measured results. Additionally, a closed-form solution was developed to estimate the worst-case envelope of the differential crosstalk.

ACKNOWLEDGMENTS

I would like to express my sincere gratitude to Dr. David Pommerenke, my advisor, for his guidance and instruction on my research work, financial support to my study and direction for this dissertation during my pursuit of the PhD's degree. I learned not only academic knowledge from Dr. Pommerenke, but also the rigorous attitude, good manners, and courage to face difficulties.

I would like to thank Dr. Jun Fan, Dr. Daryl Beetner, Dr. Victor Khilkevich, Dr. James Drewniak, and Dr. Klaus Woelk for their teaching in my courses, discussions related to my research and helpful suggestions on my dissertation.

I would also like to express my thanks to all the other faculty members and students in and out of the EMC lab for their team work and help in my coursework and research.

Finally, my heartfelt gratitude goes to my parents and my wife, Xiaoqing Wu, for their support and encouragement towards achieving this goal.

TABLE OF CONTENTS

LIST OF ILLUSTRATIONS

LIST OF TABLES

1. INTRODUCTION

In the first paper, clock and data signals in digital circuits rapidly switch between high and low levels. The switching voltage and current generate unwanted high-frequency electromagnetic fields, which interfere with receiving antennas by increasing the receiver's noise floor and reducing the receiver's sensitivity. Methods by which to minimize such de-sensitization include locating the source of the aggressor voltage and current, redesigning the aggressor circuit, and laying out the aggressor and receiving antenna in a less-coupled way. Near-field scanning enables source location by mapping the field distribution with near-field electric- and/or magnetic-field probes. The probes are key elements of the scanning technique.

To completely map the field distribution, probes should be able to detect both tangential and normal components of fields. Open-ended coaxial cable-based probes are used for normal electric field measurements. Two open-ended coaxial cables were soldered together to form a dipole-like antenna for tangential field measurement. Then, an electrically small loop was used as a magnetic field probe to measure tangential or normal components depending on the probe's orientation. In these designs, the probe's tips were either shorted or open. The input impedance of these probes is dominantly reactive with small resistance caused by losses. Without impedance matching network, the induced power is not transmitted maximally to the measurement instruments. As a result, these probes cannot easily distinguish the source from the noise when the RF interference source is weak.

RF receivers usually work in narrow frequency bands; therefore, only the interference levels in those narrow bands are of interest. For example, a camera module behaves as a noise source causing GPS receiver desensitization in a real-world cellphone. To study such problem, narrowband probes with matching impedance in the frequency band of interest are needed. Narrowband probes transmit more power to the instrument than broadband ones. Based on the matching principle, narrowband magnetic field probes have been designed that show a lower minimal detectable signal.

Magnetic field probes, however, mainly couple inductively with the currents in the circuits under test, which is helpful for locating the current source. Both the current

and voltage sources are required for building an equivalent IC noise source model. The location of the voltage source is determined using an electric field probe with capacitive coupling. Therefore, it is necessary to develop a resonant electric field probe with high sensitivity.

In this dissertation, a resonant electric field probe was designed by using transmission-line-based electric field resonators, together with cascaded quarter-wave transformers. The resonance was created by a short-ended stub inductor in parallel with an open-ended stub capacitor. The quarter-wave transformers loaded the resonator with a high impedance to achieve a high quality factor. The transformer also converted this high impedance to a low impedance of 50 Ω for the measurement instruments for maximum energy transfer. The proposed idea was validated with full-wave simulations and measurements.

In the second paper, many system integrators require that components pass radiated emissions tests before they may be used in the systems. In a typical test, for example CISPR 25, MIL-STD 461, or DO-160, the component with attached cables is placed in a semi-anechoic chamber, and radiated emissions are measured at a nearby antenna. At low frequency (e.g. 30-200 MHz) the component is generally electrically small and most emissions are caused when the attached cables are driven to radiate. While such tests are useful for evaluating the potential performance of the component within a larger system, they often cannot be performed until very late in the design cycle when engineers can make very few changes to the component design. Methods are needed to predict the radiated emissions early in the design process.

A method was presented for predicting radiated emissions from a PCB with attached cables. The cables were treated as a dipole antenna driven by a voltage across the PCB return plane. In contrast to CISCPR-25, the cables had been placed 1 m above a ground plane, thus, the horizontal polarized radiation from these cables dominated. Not taking radiation loss into account overestimated the Q-factor of the resonating structures leading to an overestimation of fields by up to 25dB.

Another approach uses full wave models to find a transfer function which relates the common-mode current on the cables to the electric field at the receiving antenna or to the receiving antenna output voltage. A transfer function can also be used to relate the

electromagnetic fields on a "Huygens-surface" of a volume surrounding the cable bundle to the receiving antenna output voltage. In order to simplify the full-wave model and reduce the simulation time, an auxiliary monopole can be used to predict fields radiated from the cables. While these techniques can generate accurate estimates of emissions, they require substantial effort and knowledge to develop the full wave model and, importantly, do not necessarily give the engineer added insight into the mechanisms that cause radiated emissions.

Emissions were modeled using a lumped-element SPICE model. The antenna was assumed to be in the near field region of the device and radiation was predicted from the capacitance between the cables and antenna. The values of the capacitors were found through numerical modeling. Although this model did a reasonably good job of predicting emissions below 300 MHz, it was not able to predict peak emissions at all frequencies, and suffered from the need to use numerical methods to predict the values of the capacitors.

This dissertation describes a method which avoids the need for numerical models and improves prediction at high frequencies. The model is intended to predict radiated emissions from component level tests, where an unshielded wire is brought out from a shielded harness bundle and runs over a return plane. This setup is common in tests used in the aerospace industry, where signal wires are shielded but the power wire is not. Common mode currents on the cables are predicted using transmission line theory. The vertical ground connections between the cables and the return plane form the radiating structures which are included as infinitesimal radiating dipoles.

Crosstalk inside the cable is another EMC issue of cable. In the third paper, cable bundles in aircraft and automotive systems consist of densely packed power signal wires mixed with high-speed data. The fields generated by one wire couple with another one nearby causing crosstalk. Models for the crosstalk help engineers predict potential issues, which is beneficial for optimizing the system design.

Available crosstalk modeling techniques are based upon multi-conductor transmission line theory with *RLGC* parameters calculated from well-defined cross sections of the multi-conductor transmission lines. Repeated cross-sectional analysis is applied to include the effect of random or systematic variations of the wire positions. The

same approach has been used to analyze the crosstalk in complex aircraft bundles, which are made primarily from shielded twisted pairs, with the addition of power wires. The disadvantage of cascading multiple transmission lines is that the cross-section geometry needs to be known in order to construct a wire representation in the cable bundle. In practice, manufacturers might not be able to provide the geometry and its range of variations. The manufacturers generally have little control of the way the cable bundles are assembled into the connectors. It has been shown that most of the coupling between the twisted pairs of the cable bundles occurs at the connectors where the shield has been removed and the wires untwisted. The parameters which determine the crosstalk within the connector are typically unknown and cannot be predicted through modeling because the position of wires within the connector is random and the connector manufacturing technique is not known. Such geometry may be extracted from X-ray scanning, but at high cost for the analysis of only a single cable bundle. Thus, it is not practical to scan every cable bundle for quality control in industrial applications. Another option is dissecting a cable assembly, which would allow the geometry of the cable to be understood. However, this does not lead to an electromagnetically relevant model without transferring the observed imperfections into an equivalent circuit model. In the early stages of design the number of available cables may also be limited, so deconstruction of the connector may not be feasible.

A measurement-based methodology was developed in prior research and extended in this dissertation to determine the crosstalk parameters within the aircraft cable connector and to model the crosstalk from a straight wire pair (e.g. power wires against the metal plane below) to shielded twisted pairs within an aircraft cable bundle. The power wires were selected because they do not have shielding layers and carry low-frequency, high-intensity signals which behave as interference sources in the aircraft and automotive systems. The method can be effective for analyzing complex aircraft cable assemblies and connectors without requiring extensive knowledge of the assembly procedure. It only uses transmission lines, mutual capacitance, and mutual inductance to predict the worst-case crosstalk up to 400 MHz.

The primary contributions of this dissertation include:

A new resonant electric field probe with higher sensitivity for RFI issues (Paper 1).

A methodology to design resonant field probe, which can be used to develop resonant E- and H-field probes at desired fixed frequencies. The design methodology can also be used to design resonant probes at tunable frequencies while the tunable frequencies can be achieved by electronically controlled components such as varactor diode. (Paper 1).

A methodology to develop an equivalent SPICE model to estimate the radiated emissions from partially shielded cables above a metal plate in component level tests. This SPICE model can be integrated into circuit simulators for circuit designers to optimize circuit designs (Paper 2).

An important finding that the ground connection from cable shields to a metal plane below the cables is mainly responsible for the emissions in the vertical direction when the height of the ground connection is electrically small. The ground connections can be represented by an array of electrically small dipoles with their radiation resistances (Paper 2).

An important finding that radiation emissions from cables above the metal plane is dominated in vertical polarization over horizontal polarization when the height of cable above the metal plane is electrically small (Paper 2).

An experimental methodology based on VNA measurements to build an equivalent circuit model to predict the single-ended and differential crosstalk between the wires inside a complex cable bundle (Paper 3).

Crosstalk of cable bundles mainly occurs inside the cable connectors where wires are exposed to each other while these wires are usually in shielded twisted pairs along the cables (Paper 3).

Crosstalk of the cable bundles mentioned above can be modeled with mutual inductance and mutual capacitance. Theses mutual coupling parameters are loaded with coupled transmission lines which represent shielded twisted pairs along the cable bundles (Paper 3).

The coupled transmission lines can change the dominant coupling mechanism between inductive coupling and capacitive coupling at different frequencies, due to transmission line effects (Paper 3).

A closed-form expression to estimate the worst-case crosstalk in the cable bundle, when the coupling mainly occurs inside the connector shell (Paper 3).

PAPER

I.   A RESONANT E-FIELD PROBE FOR RFI MEASUREMENT

Guanghua Li, *Student Member, IEEE*, Koichi Itou, Yoshihiro Katou, Noriyuki Mukai,

David Pommerenke, *Senior Member, IEEE*, Jun Fan, *Senior Member, IEEE*

ABSTRACT—Near-field probes with high sensitivity facilitate the identification of the root causes of intra-system radio frequency (RF) interference issues, where weak noise desensitizes the receiver. In the study presented in this paper, a high-sensitivity resonant electric field probe was designed, consisting of an LC resonator loaded by quarter-wave transformers for optimal power transfer at the resonant frequency. Based on the equivalent circuit model, analytical derivations and numerical simulations were performed to illustrate the design methodology. The simulation results agreed well with the measured values. At the resonant frequency of 1.577 GHz, the measured |S21| from a matched trace to the resonant probe was approximately 6.6 dB higher than that of an equivalently sized broadband probe.

Index Terms—Electric field probe, enhanced sensitivity, impedance transformer, receiver desensitization, RF interference.

1. INTRODUCTION

Clock and data signals in digital circuits rapidly switch between high and low levels. The switching voltage and current generate unwanted high-frequency electromagnetic fields, which interfere with receiving antennas by increasing the receiver's noise floor and reducing the receiver's sensitivity. Methods by which to minimize such de-sensitization include locating the source of the aggressor voltage and current, redesigning the aggressor circuit, and laying out the aggressor and receiving antenna in a less-coupled way. Near-field scanning [1-3] enables source location by mapping the field distribution with near-field electric- and/or magnetic-field probes. The probes are key elements of the scanning technique.

To completely map the field distribution, probes should be able to detect both tangential and normal components of fields. Open-ended coaxial cable-based probes are used for normal electric field measurements [4]. In [5-7], two open-ended coaxial cables were soldered together to form a dipole-like antenna for tangential field measurement. Then, in [7], an electrically small loop was used as a magnetic field probe to measure tangential or normal components depending on the probe's orientation. In these designs, the probe's tips were either shorted or open. The input impedance of these probes is dominantly reactive with small resistance caused by losses. Without impedance matching network, the induced power is not transmitted maximally to the measurement instruments. As a result, these probes cannot easily distinguish the source from the noise when the RF interference source is weak.

RF receivers usually work in narrow frequency bands; therefore, only the interference levels in those narrow bands are of interest. For example, a camera module behaves as a noise source causing GPS receiver desensitization in a real-world cellphone. To study such problem, narrowband probes with matching impedance in the frequency band of interest are needed. Narrowband probes transmit more power to the instrument than broadband ones. Based on the matching principle, narrowband magnetic field probes have been designed that show a lower minimal detectable signal [8] [9].

Magnetic field probes, however, mainly couple inductively with the currents in the circuits under test, which is helpful for locating the current source. Both the current

and voltage sources are required for building an equivalent IC noise source model [10]. The location of the voltage source is determined using an electric field probe with capacitive coupling. Therefore, it is necessary to develop a resonant electric field probe with high sensitivity.

In this paper, a resonant electric field probe was designed by using transmission-line-based electric field resonators, together with cascaded quarter-wave transformers. The resonance was created by a short-ended stub inductor in parallel with an open-ended stub capacitor. The quarter-wave transformers loaded the resonator with a high impedance to achieve a high quality factor. The transformer also converted this high impedance to a low impedance of 50 Ω for the measurement instruments for maximum energy transfer. The proposed idea was validated with full-wave simulations and measurements.

2. ELECTRIC FIELD RESONATOR

The probe was built using a four-layer printed circuit board (PCB) ($\varepsilon_r = 4.2$ and $\tan \delta = 0.02$) having a stack-up as shown in Figure 2.1 (a). This stack-up was chosen due to its low cost. Copper planes shielded the external fields and provided current return paths on the top and bottom layers, which were further connected by using the edge-plating technology. Signals were routed in the second and third layers as striplines.
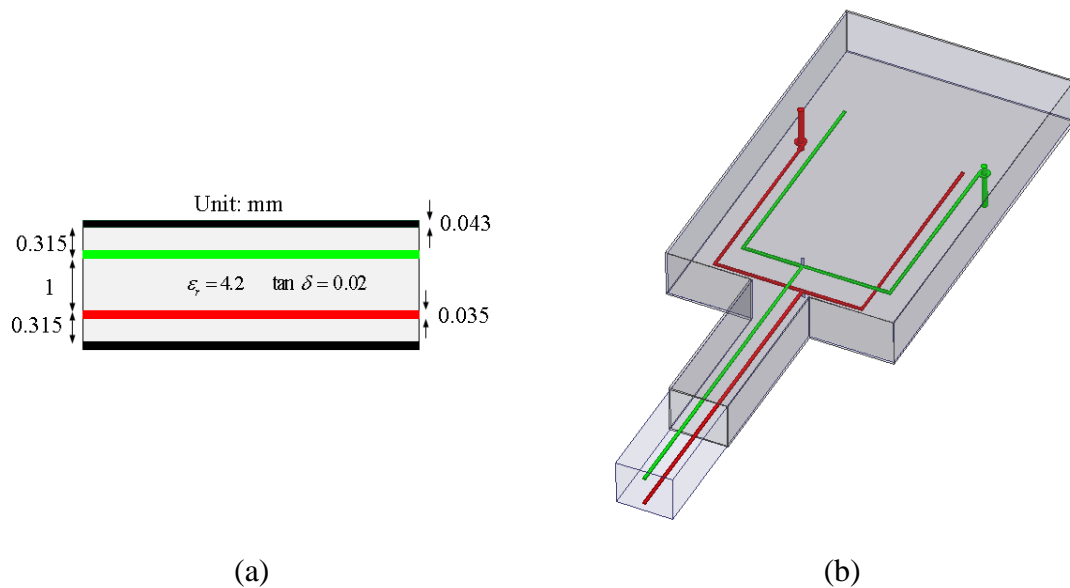
(a)   (b)

Figure 2.1. (a) PCB stack-up, (b) prospective view and (c) top view with dimensions of the Ez field resonator. Edge-plating is used to connect the coppers on the top and bottom layers. The black dash-dotted line is the axis of the PCB along the z direction. The open-ended and short-ended stubs form distributed capacitors and inductors. The traces extend 4 mm beyond the top and bottom layers, forming the probe tips.
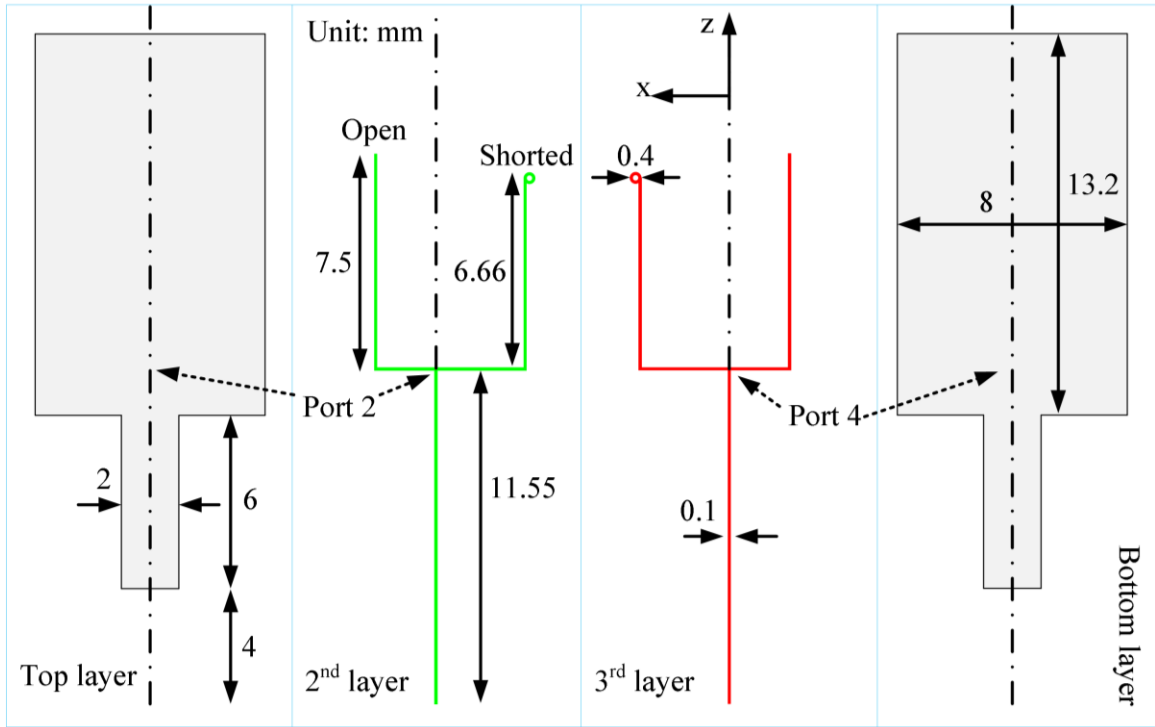
(c)

Figure 2.1. (a) PCB stack-up, (b) prospective view and (c) top view with dimensions of the Ez field resonator. Edge-plating is used to connect the coppers on the top and bottom layers. The black dash-dotted line is the axis of the PCB along the z direction. The open-ended and short-ended stubs form distributed capacitors and inductors. The traces extend 4 mm beyond the top and bottom layers, forming the probe tips (cont.).

From studies of the electric field probe based upon open-ended coaxial cables with longer inner conductors, the probe's sensitivity was proportional to the inner conductor length and cross-sectional area normal to the field polarization direction when the probe was several millimeters above a trace [11]. Similarly, in this design, two stripline traces extended 4 mm beyond the ground plane. The width of the traces was the minimal manufacturable trace width. The distance from the trace edge to the edge-plated copper was minimal, so that the probe had the smallest physical tip width with the highest spatial resolution.

Compared to a probe tip with only one stripline trace of the same size, the two-stripline tip doubled the induced voltage and maintained similar spatial resolution because the physical width of the probe tip remained the same, and the spacing of 1 mm

between them was small. Also, differential mode rejection by an via introduced in Figure 2.5 removed the H-field coupling. The resonator consisted of a short-ended stub acting as an inductor in parallel with an open-ended stub acting as a capacitor. The length and the width of the stubs determined the resonant frequency.

A 3 mm wide 50 Ω microstrip trace was used to characterize the electric field probe, which was placed 2 mm above the trace. This probe measured the electric field normal to the surface of the microstrip trace. In Figure 2.2 (a), the electric field coupling between the probe tip and the microstrip trace is represented by two capacitors, $C_{m,1}$ and $C_{m,2}$.

(a)   (b)
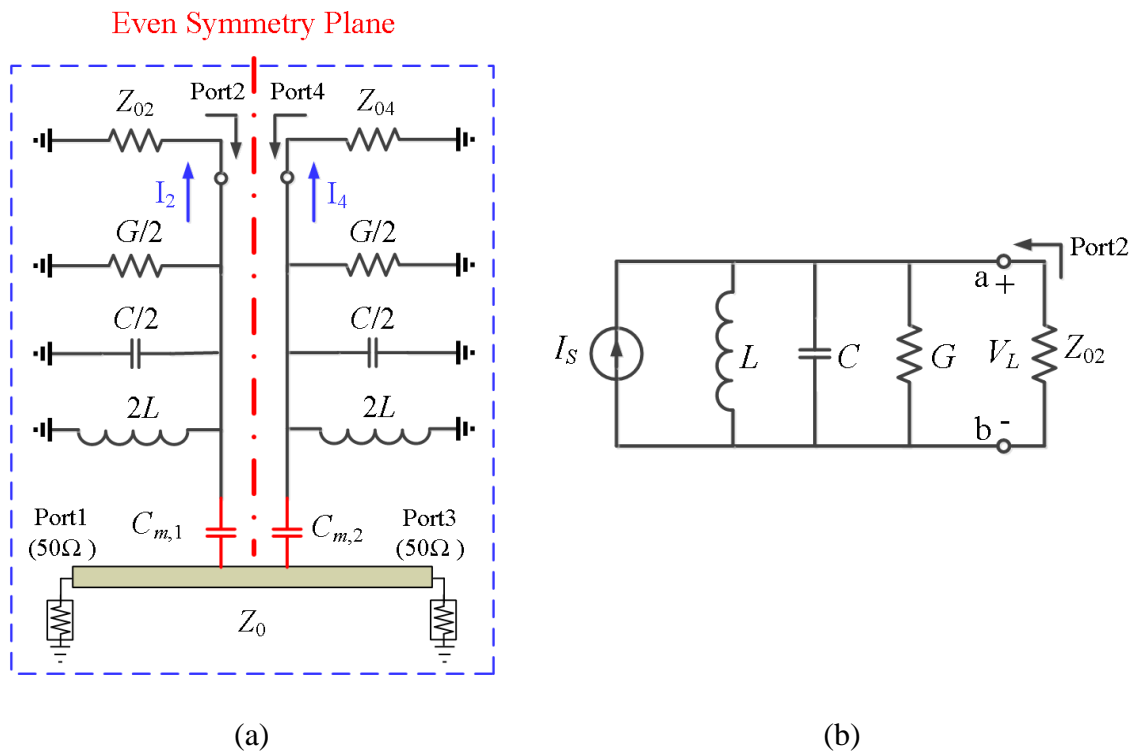
Figure 2.2. (a) Electric field resonator 2 mm above the 50 Ω microstrip trace and (b) single resonator equivalent of even-symmetrical double resonators.

In Figure 2.2, a sinusoidal source at port 1 excited the 50 Ω microstrip trace that was terminated with a matched load at port 3. The outputs of the two resonators, ports 2 and 4, were placed at the junctions of the tips and stubs as shown in Figure 2.1 (b). Ports

1 and 3 had reference impedance Z_0 (50 Ω), while ports 2 and 4 had reference impedances Z_{02} and Z_{04} ($Z_{02} = Z_{04}$, due to symmetry). Z_{02} usually does not equal Z_0, or else the resonance is damped. In the equivalent circuit model depicted in Figure 2.2 (a), shunt inductance L represents the short-ended stub in Figure 2.1 (b), shunt capacitance C represents the open-ended stub, and shunt conductance G represents the losses in the resonator, such as the conductor loss of copper and the dielectric loss of low-cost FR4.

The induced voltage at ports 2 and 4 from the electric field coupling are of the same magnitude and in phase because these ports are symmetrical. The even-mode analysis simplified the circuit in Figure 2.2 (a) to the one in Figure 2.2 (b). I_s is an equivalent current source from the electric field coupling.

When the tip size and the probe location relative to the microstrip trace are fixed, the capacitances, C_{m1} and C_{m2}, between the microstrip trace and the probe tip are constant, which determine the equivalent current source I_s. The optimal power transfer from the sources to load Z_{02} occurs when the input impedance looking into the resonator at terminals a and b is equal to the conjugate of the load impedance. At the resonant frequency, the imaginary part of the input impedance is zero. Then, the input impedance should be equal to the load impedance as $Z_{02} = 1/G$. The input impedance is large enough to make the Q factor high because the conductance caused by the dielectric loss and conductor loss is very small. This condition for the maximum power transfer is the same as that for maximum $|S_{21}|$ at the natural frequency [8]. Therefore, $|S_{21}|$ is used as the parameter for characterizing the probe's performance.

A full-wave numerical model of a probe resonator (Figure 2.1) located 2 mm above a trace was built in HFSS to extract the input impedance looking into port 2 in Figure 2.2 (a). The model contained two symmetrical resonators, which generated common-mode currents I_2 and I_4 induced from the capacitive coupling between the microstrip trace and the electric field resonator. Due to the symmetry of the structure, these two currents were of the same magnitude and in phase. The input impedance $Z_{in,p2}$ looking into port 2 in Figure 2.2 (a) can be written as

$$Z_{in,p2} = \frac{1}{G} = \left. \frac{Z_{22}I_2 + Z_{24}I_4}{I_2} \right|_{I_2 = I_4} = Z_{22} + Z_{24} \tag{1}$$

Figure 2.3 shows that the calculated $Z_{in,p2}$ reaches the maximum in magnitude (1349.5 Ω) and zero in phase at the resonant frequency, as expected for the parallel *RLC* circuit. When the impedance of the measurement instruments matches this impedance, maximum power transfer occurs. The sum of the transmission coefficients S_{21} and S_{41} also reaches the maximum. To validate this, the port reference impedance was swept from 5 Ω to 5 kΩ in the full-wave simulation. The optimal value of 1349.5 Ω was verified and used as the reference impedance at ports 2 and 4. The model in Figure 2.1 was simulated from 1 GHz to 2 GHz. The individual transmission coefficient was approximately -31.3 dB at 1.575 GHz, as shown in Figure 2.4. The summed transmission coefficient $|S_{21}+S_{41}|$ was -25.3 dB, which was 6 dB higher due to the double capacitive coupling.

(a)

(b)
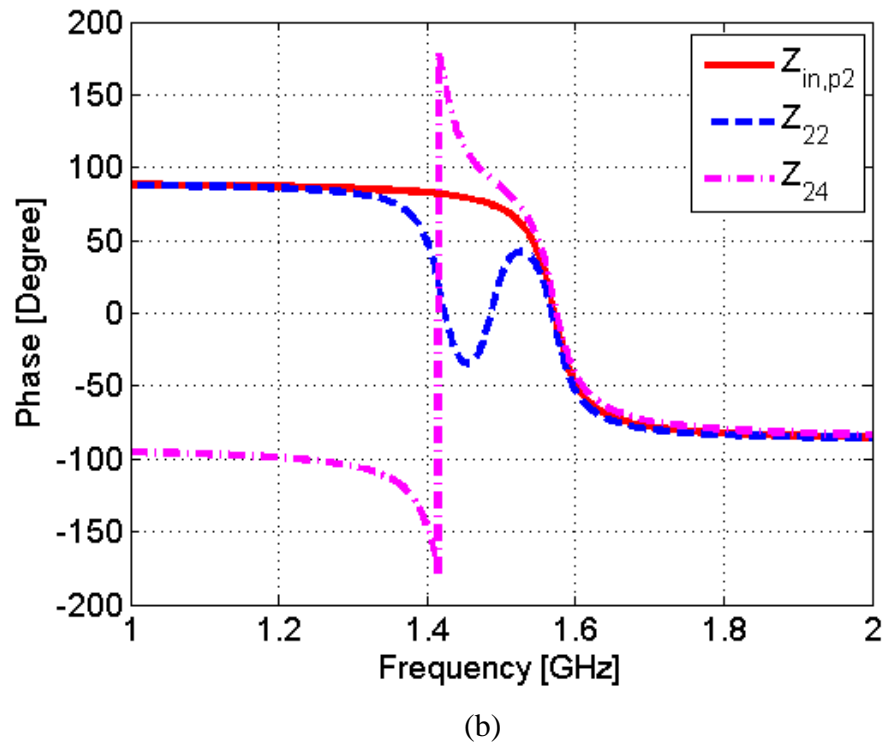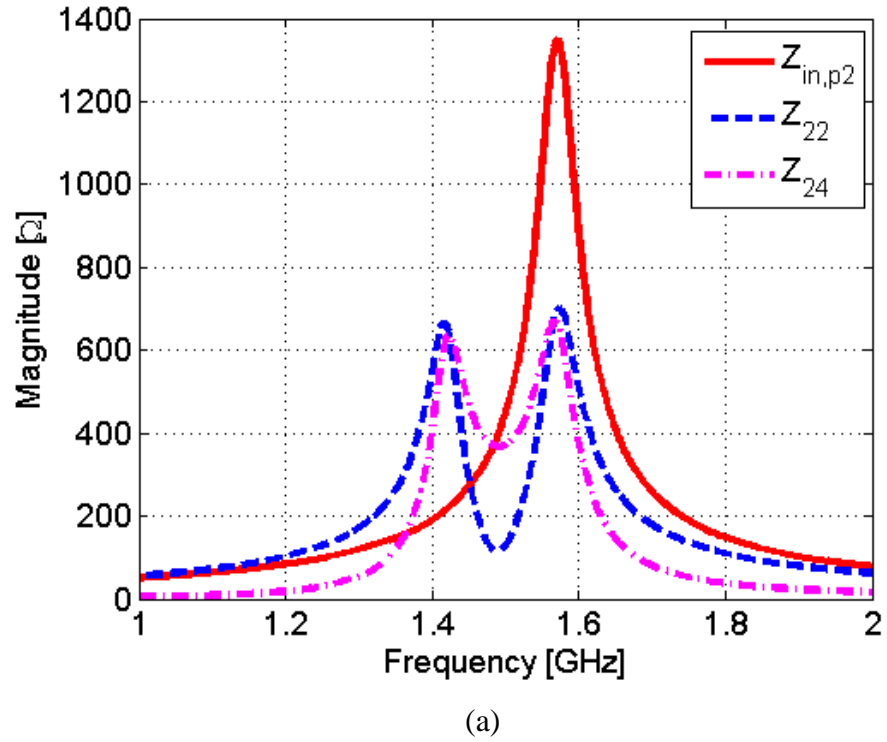
Figure 2.3. (a) Magnitude and (b) phase of the impedance looking into ports 2 and 4 of the resonator.
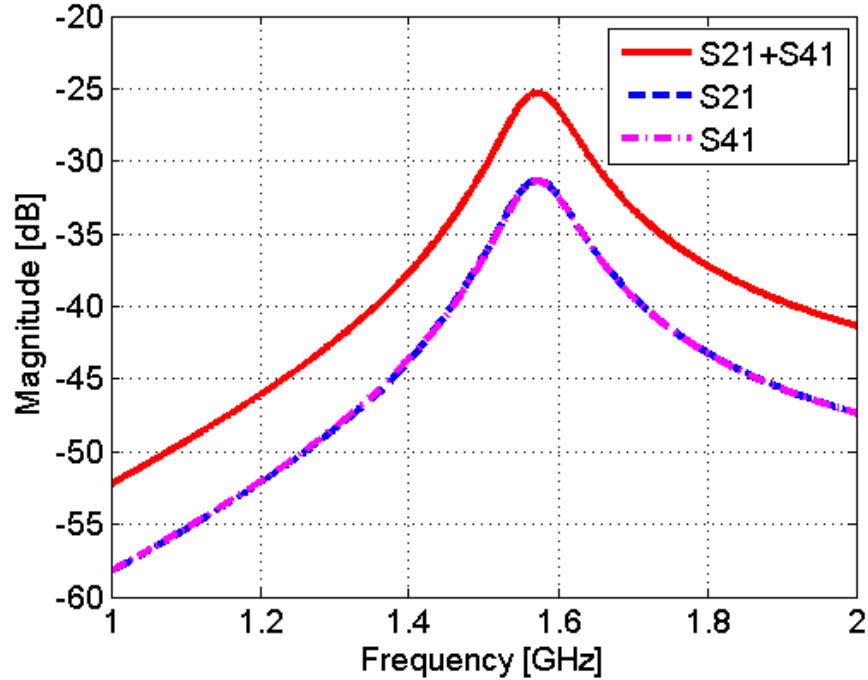
Figure 2.4. Transmission coefficients as a function of frequency at ports 2 and 4.

Ez field coupling induced the same common-mode currents, I_2 and I_4, on the two resonators, as depicted in Figure 2.2, so a via was used to combine the common-mode currents by connecting ports 2 and 4 directly. This shorted connection can also suppress the differential-mode current caused by unwanted field coupling between the trace and the resonator. Figure 2.5 illustrates the equivalent circuit model of the combined resonator. The reference impedance Z'_{02} (674.8 Ω) for port 2 was only half of the reference impedance Z_{02}.
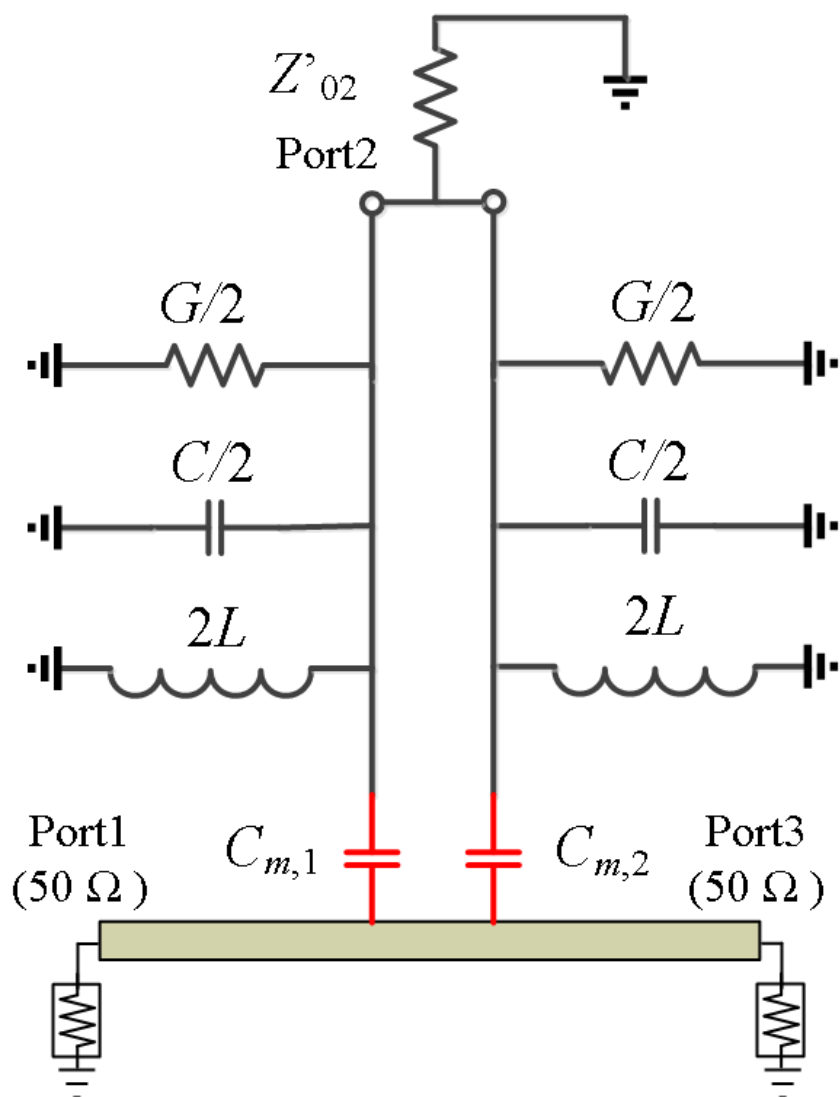
Figure 2.5. Single-ended resonator with the two individual resonators connected with a via between ports 2 and 4.

3. IMPEDANCE TRANSFORMERS

An impedance transformer was needed to transform the high impedance Z'_{02} at the resonance frequency to the low input impedance of the measurement instruments, usually 50 Ω. This was accomplished straightforwardly using quarter-wave transformers. If only one quarter-wave transformer is used, its characteristic impedance must be 183.7 Ω. However, the maximum characteristic impedance of a manufactural stripline using the stack-up shown in Figure 2.1 (a) is only 78.3 Ω. Then, two cascaded quarter-wave transformers were used. The first one was designed with a characteristic impedance of 78.3 Ω, converting 674.8 Ω to 9.1 Ω, and the second with a characteristic impedance of 21.3 Ω, transforming 9.1 Ω to 50 Ω. The dimensions appear in Figure 3.1. The simulated insertion loss of the transformer was approximately 2.1 dB at 1.575 GHz.

Unit: mm   3rd layer

$Z'_{in,p2}$ ↓ 0.1 $Z_{01} = 78.3$ Ω   ↓ 1.2 $Z_{02} = 21.3$ Ω Z_L

23.24   23.24

Figure 3.1. Dimensions of the two cascaded quarter-wave transformers in the third layer of the stack-up shown in Figure 2.1 (a).

The resonator shown in Figure 2.5 was connected to the cascaded quarter-wave transformers in Figure 3.1. The input impedance looking into the transformer with the resonator became 50.8 Ω at 1.575 GHz, as indicated in Figure 3.2. At this resonant frequency, the phase was -0.8 degrees. The resonator with the transformers was approximately purely resistive.
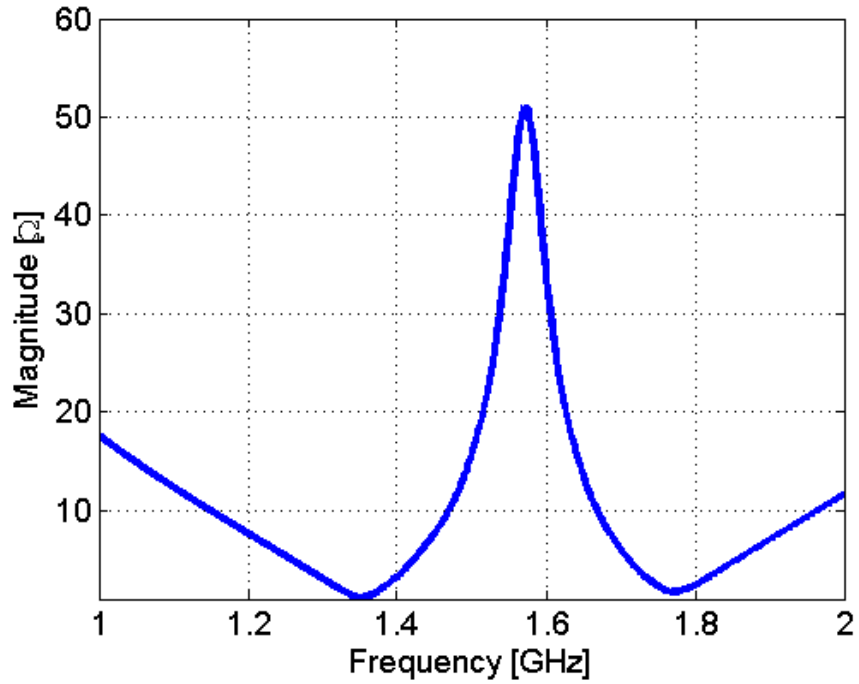
(a)
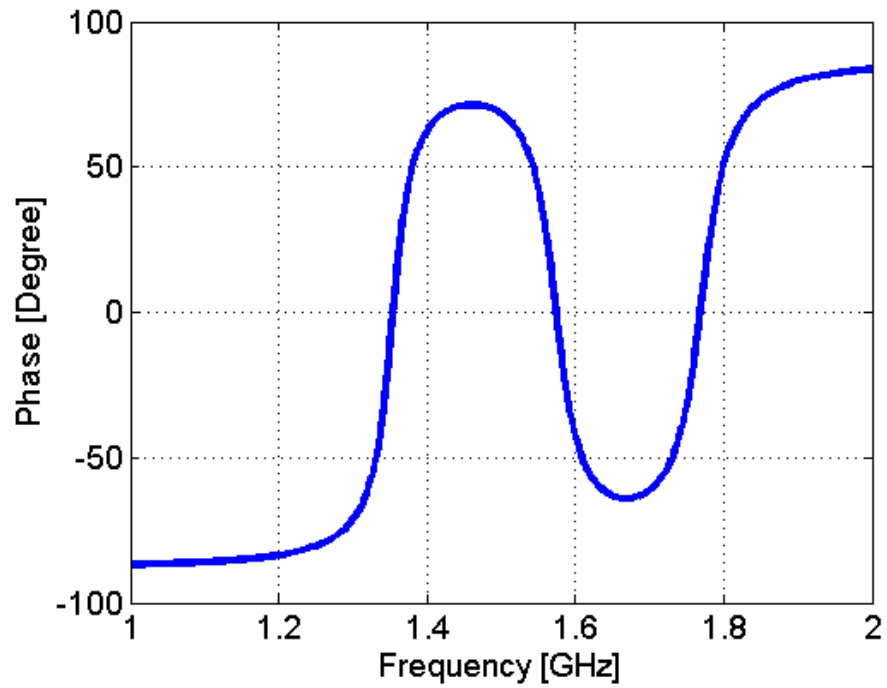
(b)

Figure 3.2. (a) Magnitude and (b) phase of the input impedance looking into the quarter-wave transformers connected with the resonator in Figure 2.5.

4. FABRICATED RESONANT AND BROADBAND PROBES

In order to demonstrate the high sensitivity of the resonant probe, both the resonant and broadband probes were fabricated. Their pictures appear in Figure 4.1. The broadband probe consisted of two stripline traces of the same size as the resonant probe. The two traces were shorted together with a via. Both probes had the same structure from the probe tip to the via. The via in the broadband probe then was cascaded with a 50 Ω stripline to the measurement instruments. However, the via in the resonant probe was loaded by LC circuits and quarter-wave transformers. $|S_{21}|$ was used to show the advantage of the resonant probe over the broadband one around the resonant frequency [8].
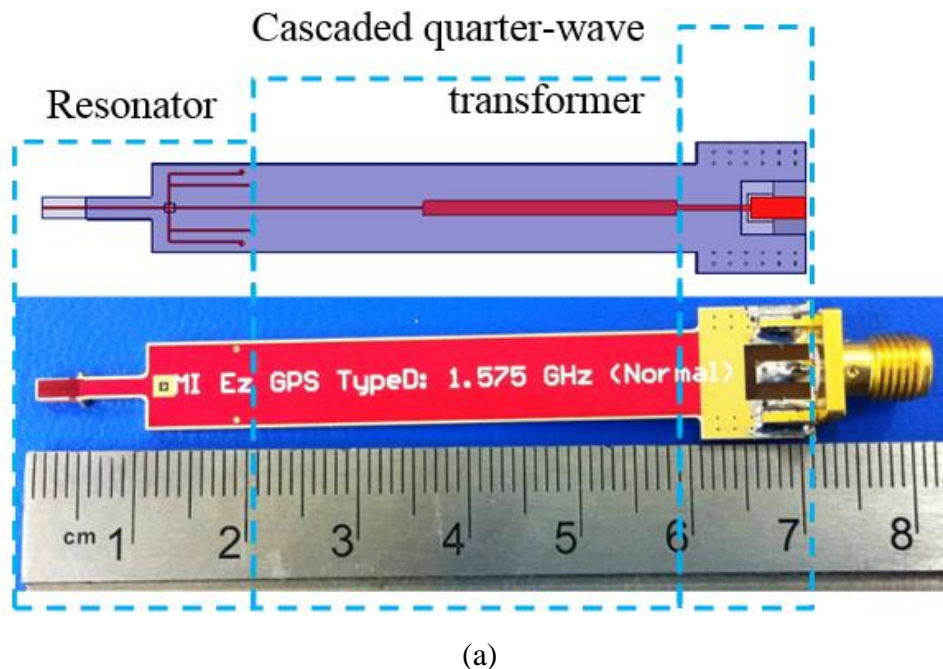
(a)

Figure 4.1. (a) Resonant probe, top: HFSS model [12], bottom: fabricated sample and (b) broadband probe, top: HFSS model, bottom: fabricated sample.

(b)
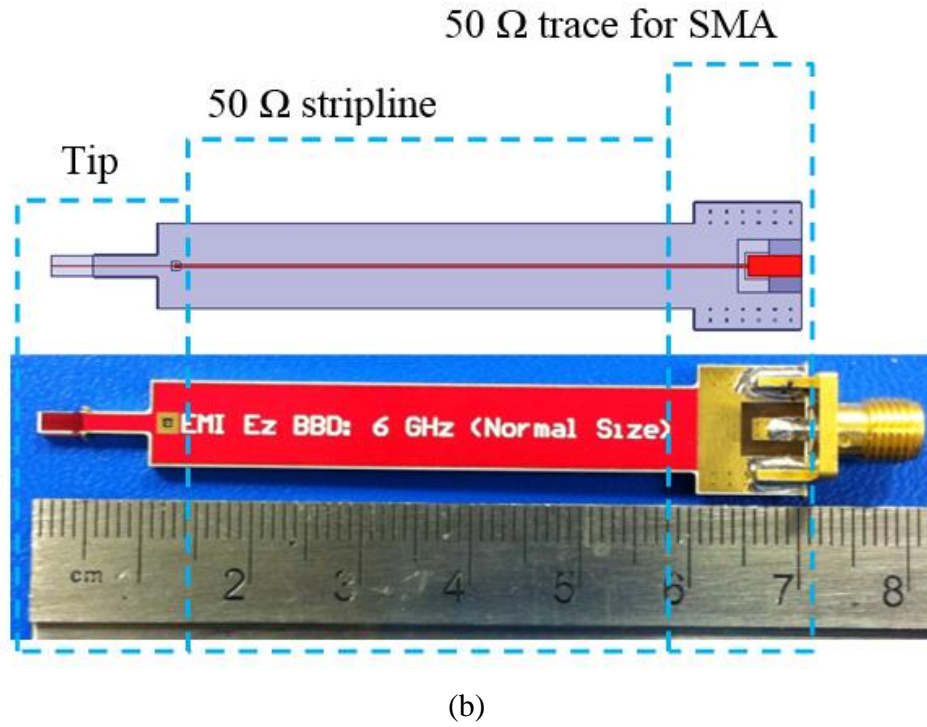
Figure 4.1. (a) Resonant probe, top: HFSS model [12], bottom: fabricated sample and (b) broadband probe, top: HFSS model, bottom: fabricated sample (cont.).

5. PROBE CHARACTERIZATION

The same measurement setup employed in [8] was used to characterize the resonant and broadband probes. A two-port vector network analyzer drove the 50 Ω matched microstrip trace from port 1. The probe was 2 mm above the top surface of the microstrip trace because this distance was of the same order as the distances used in the near-field scanning measurement [10], [13]-[16]. The coupled signal from the microstrip trace to the probes was measured at port 2 of the vector network analyzer.

Figure 5.1 illustrates that the simulated $|S_{21}|$ agreed well with the measured |S21| for the resonant probe. The simulated peak of $|S_{21}|$ occurred at -28.4 dB at 1.571 GHz, and the measured peak occurred at -28.0 dB at 1.577 GHz. Only a very small difference existed between the measured result and the simulated result. For the broadband probe, the simulated and measured results were -36.0 dB and -34.6 dB at 1.571 GHz and 1.577 GHz, respectively. Improvement was defined as the increment in the $|S_{21}|$ of the resonant probe over that of the broadband probe when both probes measured the same Ez field component. The resonant probe improved 7.6 dB in the simulation and 6.6 dB in the measurement around the resonant frequency, as listed in Table 5.1. The measured 3 dB band was 1522-1637 MHz, which covered the GPS band of 1559-1610 MHz.
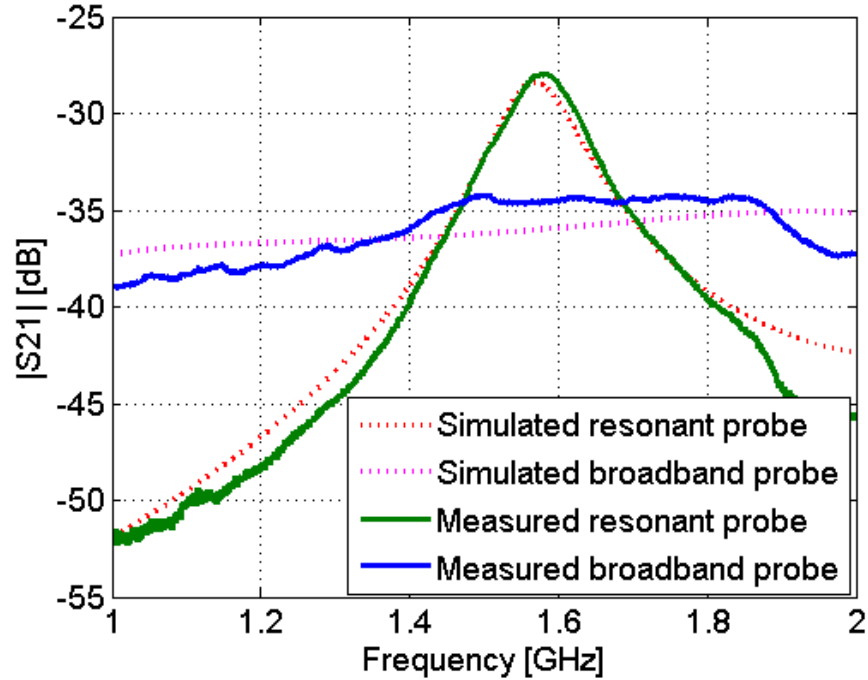
Figure 5.1. Simulated and measured transmission coefficient from a matched microstrip trace to the broadband and resonant probes.

Table 5.1. Comparison of Simulation and Measurement Results

	SIMULATION	Measurement
f_0 (GHz)	1.571	1.577
/S_{21}/ (dB)	-28.4	-28.0
Improvement (dB)	7.6	6.6

6. CONCLUSION

Based on an electric field resonator cascaded with quarter-wave transformers, a resonant electric field probe was designed with higher sensitivity than a broadband probe. The short-ended stub (inductor) and open-ended stub (capacitor) can be tuned to achieve the desired resonant frequency for the resonator. The cascaded transformer converted the high loading impedance of the resonator to the input impedance of the measurement instruments for maximum power transfer at the resonance frequency. The transmission coefficient $|S_{21}|$ from a matched microstrip trace to the probe was used as the criteria to compare the resonant and broadband probes because power was transferred maximally when $|S_{21}|$ reached its peak. The measured $|S_{21}|$ of the resonant probe was 6.6 dB higher than that of the broadband probe at the resonant frequency of 1.577 GHz. The established methodology can be used to design resonant probes with high sensitivity at different resonant frequencies.

REFERENCES

[1]   Y. Gao and I. Wolff, "Miniature electric near-field probes for measuring 3-D fields in planar microwave circuits," *IEEE Trans. Microw. Theory Tech.*, vol. 46, no. 7, pp. 907-913, Jul. 1998.

[2]   D. Baudry, C. Arcambal, A. Louis, B. Mazari, and P. Eudeline, "Applications of the near-field techniques in EMC investigations," *IEEE Trans. Electromagn. Compat.*, vol. 49, no. 3, pp. 485-493, 2007.

[3]   J. N. Reck, K. Hu, S. Li, H. Weng, D. G. Beetner, M. J. O'Keefe, D. S. Ramsay, and J. L. Drewniak, "Fabrication of two-layer thin-film magnetic-field microprobes on freestanding SU-8 photoepoxy," *IEEE Trans. Device and Mater. Reli.*, vol. 10, no. 1, pp. 26-32, Mar. 2010.

[4]   J. S. Dahele and A. L. Cullen, "Electric probe measurements on microstrip," *IEEE Trans. Microw. Theory Tech.,* vol. MTT-28, no. 7, pp. 752 -755, 1980.

[5]   H. Hosoyama, T. Iwasaki, and S. Ishigami, "Complex antenna factor of a V-dipole antenna with two coaxial feeders for field measurements," IEEE Trans. Electromagn. Compat., vol. 41, pp. 154–156, May 1999.

[6]   L. Bouchelouk, Z. Riah, D. Baudry, M. Kadi, A. Louis, and B. Mazari, "Characterization of electromagnetic fields close to microwave devices using electric dipole probes, " *Int. J. RF Microw. Comput.-Aided Eng.*, vol. 18, pp.146 - 156, 2008.

[7]   M. Kanda, "Standard probes for electromagnetic field measurements," *IEEE Trans. Antennas Propagat.,* vol. 41, no. 10, pp. 1349–1364, Oct. 1993.

[8]   H. Chuang, G. Li, E. Song, H. Park, H. Jang, Y. Zhang, D. Pommerenke, and J. Fan, "A magnetic-field resonant probe with enhanced sensitivity for RF interference applications," *IEEE Trans. Electromagn. Compat.*, vol. 55, no. 6, pp. 991-998, Dec. 2013.

[9]   G. Li, W. Huang, and D. Pommerenke, "Effect of cooling on the probe system sensitivity for low signal strength RFI problems," *in IEEE Int. Symp. Electromagn. Compat.*, Denver, CO, 2013, pp. 134-137.

[10] J. Pan, G. Li, Y. Zhou, Y. Bai, X. Yu, Y. Zhang, and J. Fan, "Measurement validation of the dipole-moment model for IC radiated emissions," *in IEEE Int. Symp. Electromagn. Compat.*, Denver, CO, 2013, pp. 666-670.

[11] D. Baudry , A. Louis and B. Mazari, "Characterization of the open-ended coaxial probe used for near-field measurements in EMC applications," *Progress Electromagn. Res.*, vol. 60, pp. 311-333, 2006.

[12] *HFSS*, ver. 13, Ansoft Corp., Pittsburgh, PA, USA, 2011. [Online]. Available: http://www.ansoft.com/.

[13] G. Li, K. Itou, Y. Katou, N. Mukai, D. Pommerenke, and J. Fan, "A resonant E-field probe for RFI measurements," *IEEE Trans. EMC*, vol. 56, no. 6, pp. 1719-1722, Dec. 2014.

[14] S. Shinde, S. Marathe, G. Li, R., Zoughi, and D. Pommerenke, "A frequency tunable high sensitivity H-field probe using varactor diodes and parasitic inductance," *IEEE Trans. EMC*., vol. 58, no. 1, pp. 331-334, 2016.

[15] G. Li, X. Zhao, and K. Huang, "A Quasi Linear Sampling Method in Electromagnetic Inverse Scattering," *Proc. of Progress in Electromagnetics Research Symposium*, March 2011.

[16] G. Li, X. Zhao, and K. Huang, "Two-dimensional imaging of three-dimensional scatterer by using Linear Sampling Method," *Proc. of International Conference on Microwave and Millimeter Wave Technology*, IEEE, pp. 1727-1730, May 2010.

II. PREDICTION OF RADIATED EMISSIONS FROM CABLES OVER A METAL PLANE USING A SPICE MODEL

Guanghua Li, *Student Member, IEEE*, Wei Qian, Andriy Radchenko, Junping He, Gary Hess, Robert Hoeckele, Thomas Van Doren, *Fellow, IEEE*, David Pommerenke, *Senior Member, IEEE*, and Daryl Beetner, *Senior Member, IEEE*

ABSTRACT—A method for creating a simple SPICE model is proposed such that the SPICE model allows prediction of radiated emissions in component level tests, such as those specified by CISPR 25 and MIL-STD 461. The model predicts measured emissions when the antenna is in the vertical direction, where emissions are typically worst for such geometry. It is shown that the radiation from the ground connections between the cables and return plane dominates over the radiation from the horizontal cables. The currents in these ground connections are predicted by treating the cables above the return plane as transmission lines and by treating the ground connections as infinitesimal radiating dipoles. The electric fields generated by these infinitesimal dipoles are summed at the antenna, where the antenna factor is then used to predict the received voltage at the antenna. Test results show this SPICE model is able to predict peak emissions within a few dB over a range from 60 MHz up to 1 GHz for a variety of circuit configurations. This model should help circuit designers better evaluate the design of their components early in the design process and help them better understand the mechanisms behind emissions problems.

Index Terms— Electromagnetic radiation, modeling, SPICE, cables, testing.

1. INTRODUCTION

Many system integrators require that components pass radiated emissions tests before they may be used in the systems. In a typical test, for example CISPR 25, MIL-STD 461, or DO-160, the component with attached cables is placed in a semi-anechoic chamber, and radiated emissions are measured at a nearby antenna [1]-[3]. At low frequency (e.g. 30-200 MHz) the component is generally electrically small and most emissions are caused when the attached cables are driven to radiate [4]. While such tests are useful for evaluating the potential performance of the component within a larger system, they often cannot be performed until very late in the design cycle when engineers can make very few changes to the component design. Methods are needed to predict the radiated emissions early in the design process.

A method was presented in [5] for predicting radiated emissions from a PCB with attached cables. The cables were treated as a dipole antenna driven by a voltage across the PCB return plane. In contrast to CISCPR-25, the cables had been placed 1 m above a ground plane, thus, the horizontal polarized radiation from these cables dominated. Not taking radiation loss into account overestimated the Q-factor of the resonating structures leading to an overestimation of fields by up to 25dB.

Another approach uses full wave models to find a transfer function which relates the common-mode current on the cables to the electric field at the receiving antenna [6] or to the receiving antenna output voltage [7]. A transfer function can also be used to relate the electromagnetic fields on a "Huygens-surface" of a volume surrounding the cable bundle to the receiving antenna output voltage [8], [9]. In order to simplify the full-wave model and reduce the simulation time, an auxiliary monopole can be used to predict fields radiated from the cables [10]. While these techniques can generate accurate estimates of emissions, they require substantial effort and knowledge to develop the full wave model and, importantly, do not necessarily give the engineer added insight into the mechanisms that cause radiated emissions.

Emissions were modeled in [11] using a lumped-element SPICE model. The antenna was assumed to be in the near field region of the device and radiation was predicted from the capacitance between the cables and antenna. The values of the

capacitors were found through numerical modeling. Although this model did a reasonably good job of predicting emissions below 300 MHz, it was not able to predict peak emissions at all frequencies, and suffered from the need to use numerical methods to predict the values of the capacitors.

This paper describes a method which avoids the need for numerical models and improves prediction at high frequencies. The model is intended to predict radiated emissions from component level tests, where an unshielded wire is brought out from a shielded harness bundle and runs over a return plane. This setup is common in tests used in the aerospace industry, where signal wires are shielded but the power wire is not [2]. Common mode currents on the cables are predicted using transmission line theory. The vertical ground connections between the cables and the return plane form the radiating structures which are included as infinitesimal radiating dipoles.

2. SIMPLIFIED TEST SETUP FOR RADIATED EMISSIONS

Figure 2.1 shows the radiated emissions test setup for a MIL-STD 461 test [2]. The component – or device under test (DUT) - sits in a shielded enclosure, on top of a large metallic return plane. The DUT drives a harness of shielded cables. The harness is 5 cm above the return plane. An unshielded power wire runs with the harness to a point in the center of the table, where the power wire is separated from the harness to connect with a Line Impedance Stabilization Network (LISN). At the point where the power wire separates from the rest of the harness, the harness shield(s) are connected to the return plane with a ground connection. The cables are placed 10 cm from the edge of the return plane and 1 m from a biconical antenna. The cable harness and unshielded power wire are both run along the edge of the table for 1 m. Since the DUT is well shielded and the harness shields are well-connected to the DUT enclosure, only the currents on the power wire are expected to drive emissions. A similar setup is used in CISPR 25 tests [1].
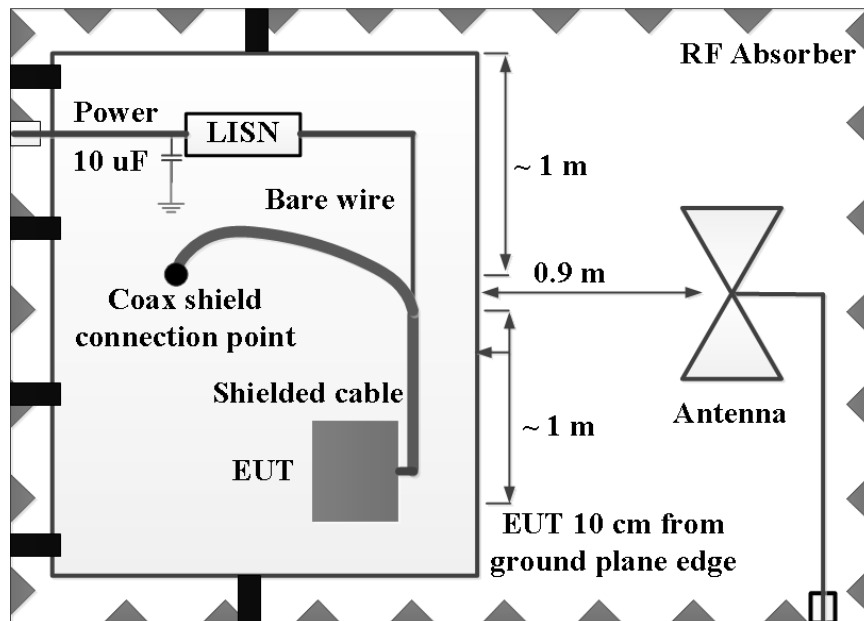
Figure 2.1. Test setup used to measure radiated emissions from the component with attached cables, according to standard tests [1]-[3].

Figure 2.2 shows a simplified test setup that was used to develop an equivalent circuit model for predicting radiated emissions. The shielded cable in Figure 2.1 was replaced with a 1 m long coaxial cable as shown in Figure 2.2 (a) and Figure 2.2 (b). The power wire was represented with a single 1 m long bare wire terminated to the return plane. The bare wire was connected to the center conductor of the shielded cable as shown in Figure 2.2 (b), where the power wire would be pulled out from the harness of shielded cables. The shield of the coaxial cable was terminated to a metal bracket at location $x = x_1$ in Figure 2.2 (b) to represent the shield's connection to the DUT and was shorted to the return plane with a strip of copper tape where the bare wire leaves the cable (at $x = x_2$). The load termination for the bare wire was modified for different tests, though in the typical test the bare wire was shorted to the return plane with a strip of copper tape, since this termination generated the worst case emissions.

The coaxial cable was driven by a vector network analyzer (VNA) representing the noise driven by the DUT as shown in Figure 2.2 (b). A biconical antenna was located 1 m from the point where the coaxial cable and power wire separated, as shown in Figure 2.2 (c). Radiated emissions were represented from the values of S_{21} between the port driving the shielded cable, and the port connected to the output of the antenna.
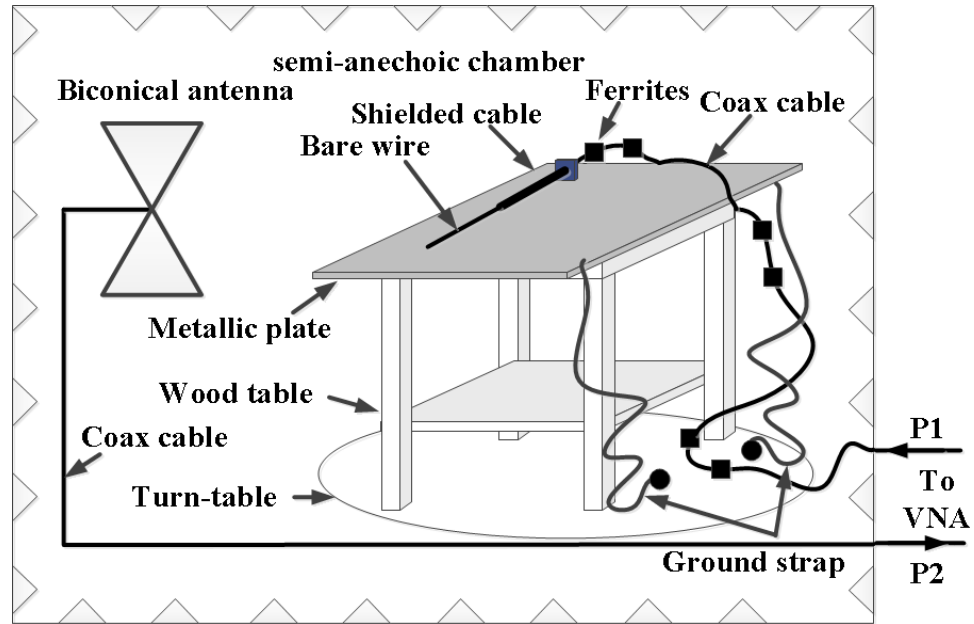
(a)
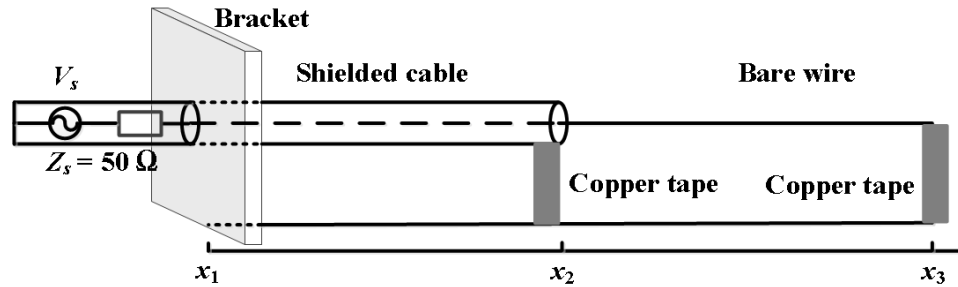
(b)
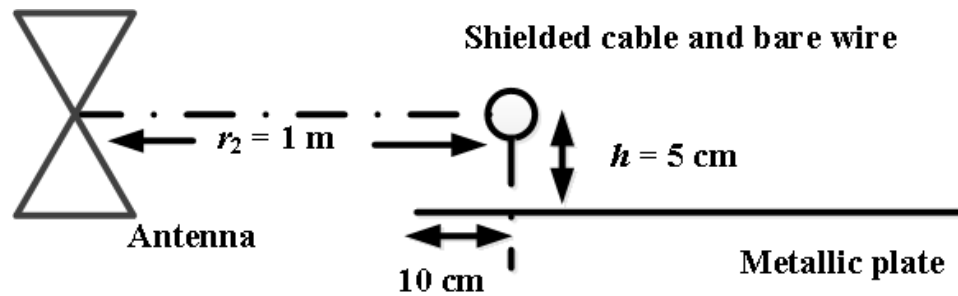
(d)

Figure 2.2. Simplified setup used to develop an equivalent circuit model of radiated emissions: (a) Position of components within the semi-anechoic chamber; (b) Close-up of shielded cable and of bare wire driven by a noise voltage source (here from the VNA); (c) Relative position of cables and antenna.

Previous work has shown that the emissions measured by a vertically polarized antenna are higher than by a horizontally polarized antenna for this setup, as shown in Figure 2.3 [11]. This paper focuses on the worst emissions, so models were developed only for the vertical polarization.
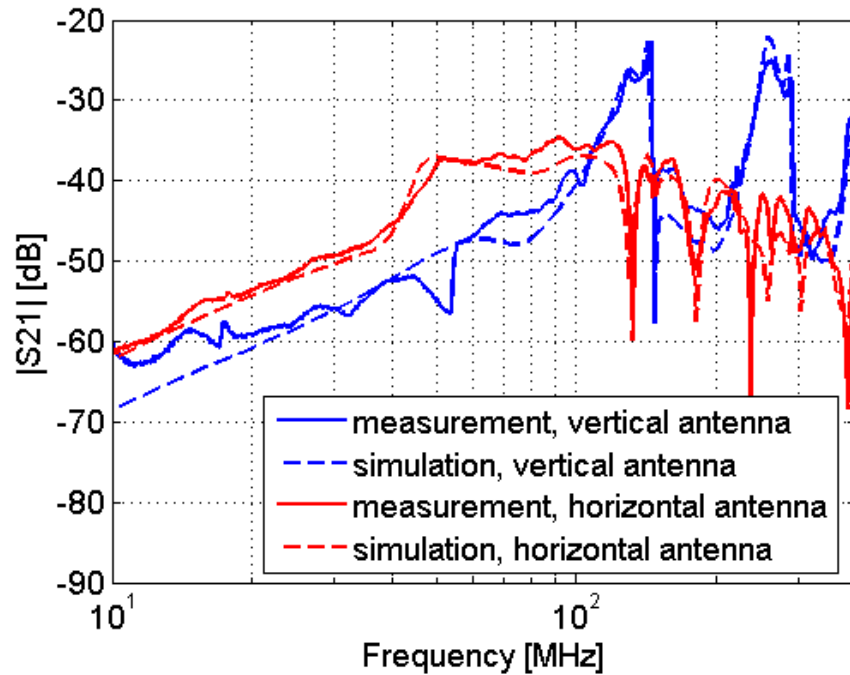
Figure 2.3. Comparison of $|S_{21}|$ for vertically and horizontally polarized receiving antennas when the bare wire is shorted to the metal plate in Figure 2.2 (b).

3. MODELING PROCEDURE

3.1. COMMON-MODE VOLTAGE SOURCE

The radiated emissions are driven by common mode currents on the bare wire, the shield, and the connections to the return plane. The bare wire is driven by the voltage between the shield and the bare wire at junction $x = x_2$, where the power wire leaves the shielded cable harness. This voltage can be modeled as being generated by a noise voltage source V_s with source impedance R_s. This noise source is within the DUT at $x = x_1$ as shown in Figure 2.2 (b). When the source impedance R_s is equal to the characteristic impedance Z_0 of the shielded cable, the source at $x = x_2$ is a phase shifted version of the source at $x = x_1$ with the same magnitude.

$$V_s (x = x_2) = V_s (x = x_1)e^{-j\beta l} \tag{1}$$

Since we are only interested in the magnitude of the radiated emissions, the phase of the voltage source can be ignored, and the source voltage can be placed directly at $x = x_2$ as shown in Figure 3.1. When V_s is 2 V, Z_s is 50 Ω, and the antenna output is loaded with 50 Ω, the magnitude of the voltage at the antenna output is equivalent to the magnitude of S_{21} [11].
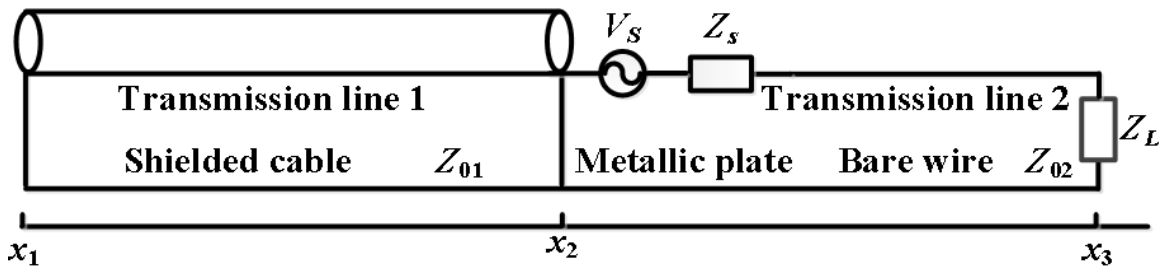
Figure 3.1. The setup in Figure 2.2 can be simplified as two transmission lines driven by a voltage source placed between the cable shield and the bare wire.

3.2. TRANSMISSION LINE MODEL FOR THE CABLES

While the transmission line formed by the inner conductor of the coaxial cable and its shield can be ignored by shifting the source to location $x = x_2$, the transmission line formed by the coaxial cable shield above the return plane cannot be ignored. The shield above the return plane and the bare wire above the return plane were both treated as transmission lines. The transmission line formed by the bare wire is driven directly by the source voltage, as illustrated in Figure 3.1. The transmission line formed by the shield above the return plane is driven through inductive coupling. Modeling the transmission line formed by the cable shield is critical, since there is very little loss in this transmission line and substantial resonances can occur.

The characteristic impedance of the transmission lines, Z_{0i} (i=1, 2) in Figure 3.1, can be determined from the formula [13]

$$Z_{0i} = 60 \cosh^{-1}\left(\frac{2h}{D_i}\right) \tag{2}$$

where h is the distance from the center of the conductor to the metal plane, and D_i is the diameter of the conductor, where i=1 for the shield and i=2 for the bare wire. The electrical length of the transmission line can be represented by a time delay, $t_{d,i}=l_i/v_0$, where l_i is the length of the transmission line, and v_0 is the speed of light in air, since air fills in the space between the shield or bare wire and the metallic plate.

3.3. INDUCTANCE OF VERTICAL CONDUCTOR SEGMENTS

The cable shield and the bare wire are both shorted to the metallic plate with a metal bracket or a piece of copper tape as illustrated in Figure 2.2 (b). The contribution of these vertical grounding conductors to the circuit was not accounted for in the transmission line model in Figure 3.1. The primary contribution of the vertical grounding conductors is through inductance. While inductance is a property of loops, the inductance contributed by one part of the loop can be approximated using partial self- and mutual-inductances. The vertical conductors are relatively far apart so their partial mutual-

inductance can reasonably be ignored and the partial self-inductance of the vertical conductors can be used to approximate the contribution of these conductors to the overall inductance.

Let the partial self-inductance of the bracket at $x = x_1$ in Figure 2.2 (b) be L_1, and the partial self-inductances of the copper tape at $x = x_2$ be L_2 and at $x = x_3$ be L_3. The vertical conductors are electrically small from 30 MHz to 200 MHz, so the current density is approximately constant throughout the segments. The self-inductances of the copper tape, L_2 and L_3, can be calculated using the equation for a thin rectangular conductor [14],

$$L_2 = L_3 = \frac{0.002}{3w^2}\left[\begin{array}{l} 3w^2 l \ln\dfrac{l + \sqrt{l^2 + w^2}}{w} - \left(l^2 + w^2\right)^{3/2} \\ \\ + 3l^2 w \ln\dfrac{w + \sqrt{w^2 + l^2}}{l} + l^3 + w^3 \end{array}\right] \text{u H} \tag{3}$$

where w is the width of the copper tape in cm, and l is the length in cm. For the bracket, with a thickness-to-width ratio less than 0.1, the self-inductance can be calculated as [14],

$$L_1 = L_2 - Kl\frac{t}{w}10^{-3} \tag{4}$$

where t is the bracket thickness in cm, and K=2.05 is a constant.

3.4. RADIATION RESISTANCE

Modeling radiation loss is critical as the transmission line formed by the shielded cable has almost no other source of loss and thus can exhibit high-Q resonances. The majority of radiation is caused by the vertical ground connections. While the cables above the return plane may radiate, their radiation efficiency is small since the wires are electrically close to the return plane [11]. On the other hand, while the grounding conductors are short, they are electrically far apart so they can radiate without interfering with one another. The electric field from the currents in the ground conductors can be

estimated using a Hertzian dipole. In the SPICE model, the radiated loss of the Hertzian dipole is represented through its radiation resistance. Let the vertical conductor segments be an infinitesimal dipole from 30 MHz to 200 MHz. Its radiation resistance, R_{rad}, can be approximated as [15]

$$R_{rad} = 80\pi^2\left(\frac{h}{\lambda}\right)^2 \tag{5}$$

where λ is the wavelength in air. All three segments were assumed to have the same radiation resistance, since they have the same height.

3.5. OVERALL MODEL AND RESULTING ELECTRIC FIELD

The overall SPICE model used to predict currents within the test setup is shown in Figure 3.2. The equivalent source voltage was set to 2 V and source impedance to 50 Ω, to represent the VNA source used in measurements. The transmission line with characteristic impedance Z_{01} represents the shielded cable. The transmission line with characteristic impedance of Z_{02} represents the bare wire. Three inductors, L_1, L_2, and L_3, are the self-inductances of the vertical conductor segments. R_{rad} is the radiation resistance of the Hertzian dipoles associated with the vertical ground conductors. The metallic plate is represented by the GND connection. The reference direction of currents I_1, I_2 and I_3 is from the metallic plate to the cables.
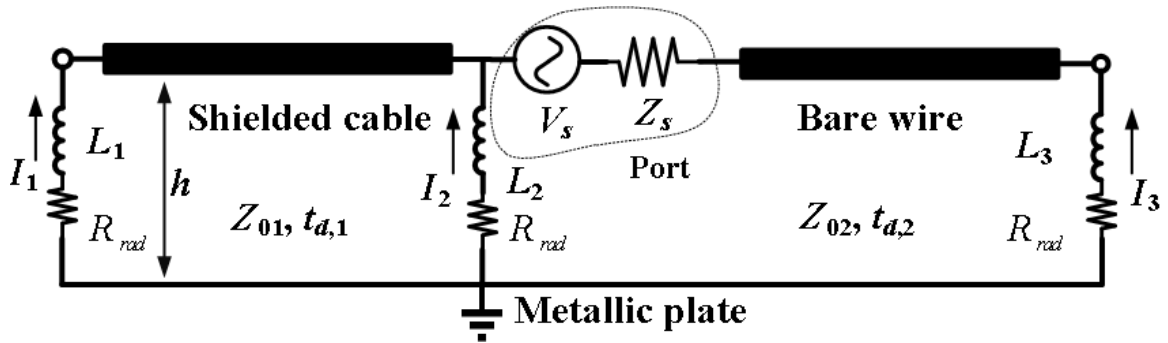
Figure 3.2. The SPICE model used to determine currents in the ground conductors, I_1, I_2 and I_3.

The Hertzian dipoles representing the vertical grounding conductors generate radiated emissions in the vertical polarization. The vertically polarized electric field from a single dipole is given by

$$E_{z,i} = -\frac{I_i h}{4\pi}\eta_0\beta_0^2 \sin(\theta)\left(j\frac{1}{\beta_0 r_i} \right)e^{-j\beta_0 r_i} \tag{6}$$

where $\vec{I}_i = \hat{z}I_i$ are the currents in the grounding conductors i (i=1, 2, 3), $\eta_0 = 377\ \Omega$ is the wave impedance in free space, $\beta_0 r = 2\pi r / \lambda_0 = 2\pi r f_0 / v_0$ is the electrical distance from the dipole to a biconical antenna, and $\theta = 90^0$ is the polar angle. Each current is constant in space and is frequency dependent. The vertically polarized biconical antenna is located at $P(x, y, z) = (0, 1, 0)$, as shown in Figure 3.3.
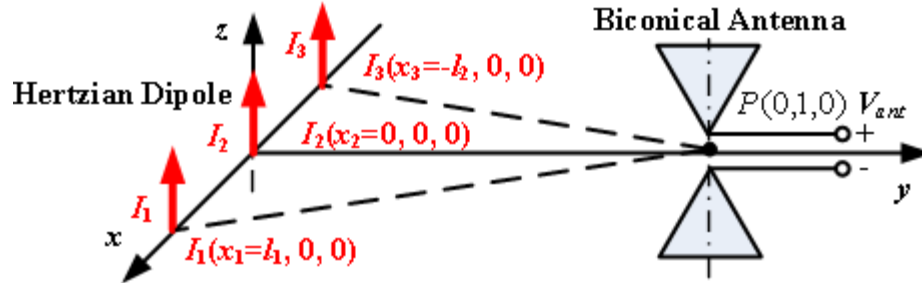
Figure 3.3. A vertically polarized biconical antenna receives the radiated fields from three Hertzian dipoles located along the x-axis.

The reflection from the metal plate was ignored when estimating fields because the dipoles are only 10 cm away from the edge of the plate. In addition, nearly half of the antenna is below the plate. Simulations were used to validate this assumption. Using superposition, the total electric field at the observation point P is given by

$$E_z = \sum_{i=1}^{3} E_{z,i} \tag{7}$$

3.6. ANTENNA FACTOR OF BICONICAL ANTENNA

Experiments were performed with a biconical antenna (Schwarzbeck Mess-Elektronik balun no. VHBB 9124 and elements BBA 9106). The antenna factor was determined by the manufacturer in an open area test site using the three-antenna method [16]. The antenna datasheet only provided the magnitude of the antenna factor at 1 m and 5.3 m from 30 MHz to 300 MHz. While this is the primary range of interest, the model was tested at both higher and lower frequencies (marked with shading in the figures below) to better demonstrate its capabilities. A full-wave model of the antenna was already available in our laboratory [11] [17]. This full wave model was used to determine the antenna factor for a greater frequency range than was available in the datasheet. The antenna factor was calculated as

$$\left| AF \right| = E_{z,dBuV/m} - V_{ant,dBuV} \quad [dB/m] \tag{8}$$

where E_z is the simulated z-component of the electric field generated by a Hertzian dipole I_2 in Figure 3.3 at the observation point $P(x, y, z) = (0, 1, 0)$ or $P(x, y, z) = (0, 5.3, 0)$ without the presence of the receiving biconical antenna, and V_{ant} is the induced output voltage at the antenna terminals.

This full-wave model does not take into account multiple reflections between the antenna and the semi-anechoic chamber walls, since they are small. Figure 3.4 shows the magnitude of the estimated antenna factor at 1 m and 5.3 m. The simulated antenna factor matches the antenna factor from the datasheet from 40 MHz to 300 MHz within a few decibels. Some difference was observed from 25 MHz to 40 MHz. This difference is caused by a difference in the simulation and measurement setups. While no measurement was performed to validate the model outside of this frequency range, the close match from 40 MHz to 300 MHz gives confidence in the model.
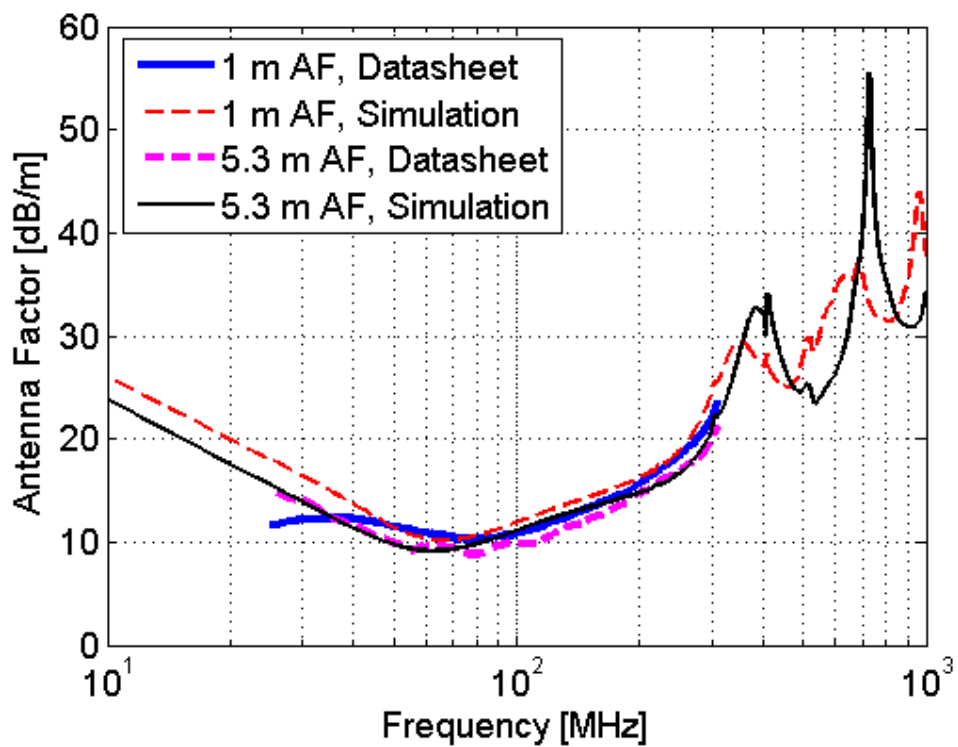
Figure 3.4. Magnitude of the antenna factor at 1 m and 5.3 m. Areas outside the test limits are shaded.

4. VALIDATION

The equivalent circuit model was validated against measurements and simulations while varying the length of the bare wire, the height of the wires above the return plane, and the distance between the cables and the antenna. Table 4.1 lists the circuit parameters used for the conventional setup, shown in Figure 3.2. The values of the parameters are either measured or calculated from the geometry and equations mentioned above, without any parameter tuning.

The currents in the vertical grounding conductors were found in SPICE using the model shown in Figure 3.2. The radiated electricfield at the antenna was then calculated using (7) in Matlab. Since the induced voltage at the antenna terminals is equal to the transmission coefficient from the noise source to the antenna terminals, S_{21} can be calculated from (8) as

$$| S21 | [dB] = \left. \left| E_z \right| \right|_{dB\,\mu V\,/\,m} - AF_{dB\,/\,m} - 120 \tag{9}$$

when the circuit is driven by a 2 V source with a 50 Ω source impedance, as in Figure 3.2.

The magnitude of the radiated emissions, given by $|S_{21}|$, is shown in Figure 4.1 as predicted by the proposed SPICE model, as predicted by a full wave model, and as measured in a semi-anechoic chamber. The accuracy of the full wave model was previously demonstrated in another paper [11] and matches measurements within a few dB from 10 MHz – 1 GHz. This good match suggests the full wave model can be trusted in later experiments where measurements were not performed. The resonance frequencies are approximately the same for the SPICE model and full wave model and measurement. These resonances occur when the cables are approximately a half wave length long and the current in the loop reaches a maximum [11]. Values of $|S_{21}|$ peak at the resonant frequencies. The model does not work well below 60 MHz, because the cables are electrically short and radiation is weak. The emissions at these low frequencies are typically much weaker than at high frequencies so are not usually an issue.

Table 4.1. Parameter Settings for the Model in Figure 3.2

V_s (V)	2	D_1 (mm)	5	l_1 (m)	1.01
Z_s (Ω)	50	D_2 (mm)	2	l_2 (m)	1.07
L_1 (nH)	10.1	Z_{01} (Ω)	179.5	$t_{d,1}$ (ns)	1.6833
L_2, L_3 (nH)	24.9	Z_{02} (Ω)	234.5	$t_{d,2}$ (ns)	1.7834
h (cm)	5	r_2 (m)	1	R_{rad}	Eqn. (5)

Figure 4.1. Comparison of the measured, simulated (full-wave model), and predicted (SPICE) values of $|S_{21}|$ between the cables and the antenna located 1 m away. Values were found using the parameters in Table 4.1.

Additional tests were made using the parameters listed in Table 4.2. Parameters not shown in Table 4.2 were as given in Table 4.1. Figure 4.2 shows the measured, simulated, and predicted values of $|S_{21}|$ for configuration 2. As the bare wire is shortened to 0.8 m, the resonance at about 130 MHz in Figure 4.1 was shifted to roughly 187 MHz. The resonance frequency related to the shielded cable does not shift, however, as its

length did not change. As in Figure 4.1, the predicted values of $|S_{21}|$ closely match those from full wave simulations above 60 MHz.

Table 4.2. Modified Test Configurations

Configuration 2	l_2 (m)	0.8	$t_{d,2}$ (ns)	1.3334
Configuration 3	l_2 (m)	0.8	$t_{d,2}$ (ns)	1.3334
	h (cm)	10	L_1 (nH)	29.4
	L_2, L_3 (nH)	62.8		
Configuration 4	r_2 (m)	5.3		
Configuration 5	l_2 (m)	0.8	$t_{d,2}$ (ns)	1.3334
	r_2 (m)	5.3		
Configuration 6	h (cm)	10	L_1 (nH)	29.4
	L_2, L_3 (nH)	62.8	r_2 (m)	5.3
Configuration 7	l_2 (m)	0.8	$t_{d,2}$ (ns)	1.3334
	h (cm)	10	L_1 (nH)	29.4
	L_2, L_3 (nH)	62.8	r_2 (m)	5.3

Figure 4.2. Comparison of the measured, simulated (full-wave), and predicted (SPICE) values of $|S_{21}|$ between the cables and the antenna found using the parameters settings for configuration 2 in Table 4.2.

Figure 4.3 shows the simulated and predicted values of $|S_{21}|$ for configuration 3, where both the shielded cable and the bare wire were lifted to a height of 10 cm above the metallic table. The full-wave model and predicted values of S21 match within a few decibels above 60 MHz. When the height increases, the characteristic impedance of the transmission lines in (2), the load "inductance" in (3) and (4), and the radiation resistance in (5) all increase. The length of the dipole also increases. These effects cause the dipole moment to increase, so one would expect larger emissions in the vertical polarization for this configuration than for the previous configurations, as is clear when comparing Figure 4.2 and 4.3.
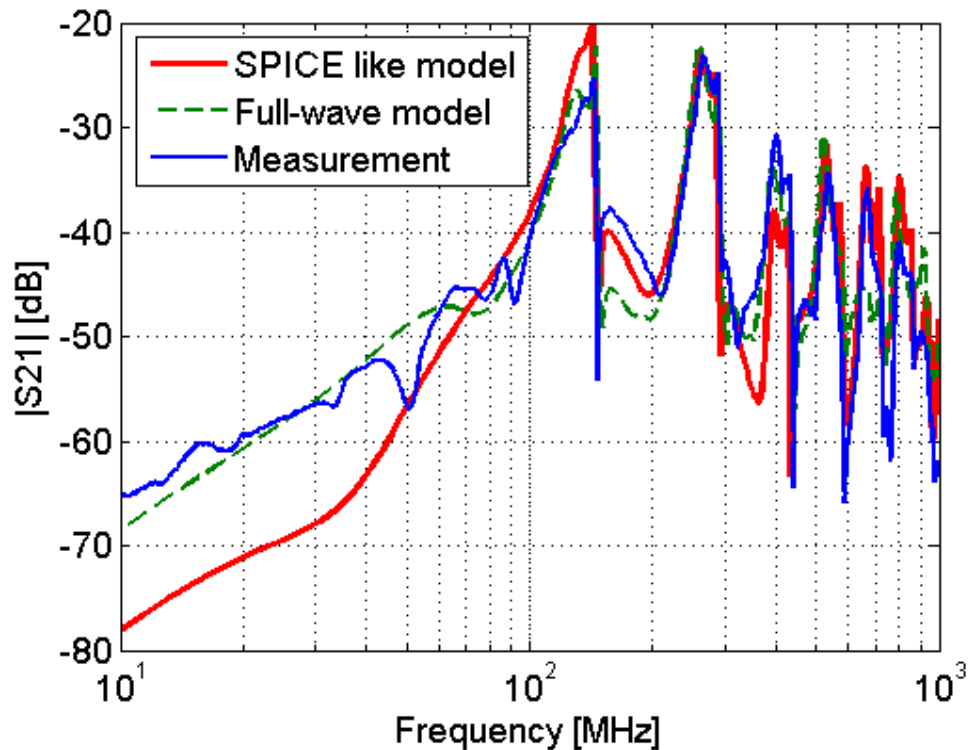
Figure 4.3. Comparison of the measured, simulated (full-wave), and predicted (SPICE) values of $|S_{21}|$ between the cables and the antenna found using the parameters settings for configuration 3 in Table 4.2.

In configurations 4-7, the antenna was moved to 5.3 m away from the experimental setup. Since the electric field is inversely proportional to the distance, as shown in (6), the emissions are expected to weaker, though the overall shape of the emissions with frequency is expected to be similar (neglecting changes in the phase of the electric field at the antenna for the three grounding conductors as the antenna is moved further away). Figure 4.4 to Figure 4.7 show the simulated and predicted emissions for these configurations. As expected, emissions were smaller than for similar configurations with a closer antenna. The difference of results between SPICE and full-wave models at low frequency is smaller when the antenna is farther away. For example at 20 MHz the difference is 10 dB in Figure 4.1, while 8 dB in Figure 4.4. The proposed model did a good job of predicting the emissions at this distance.
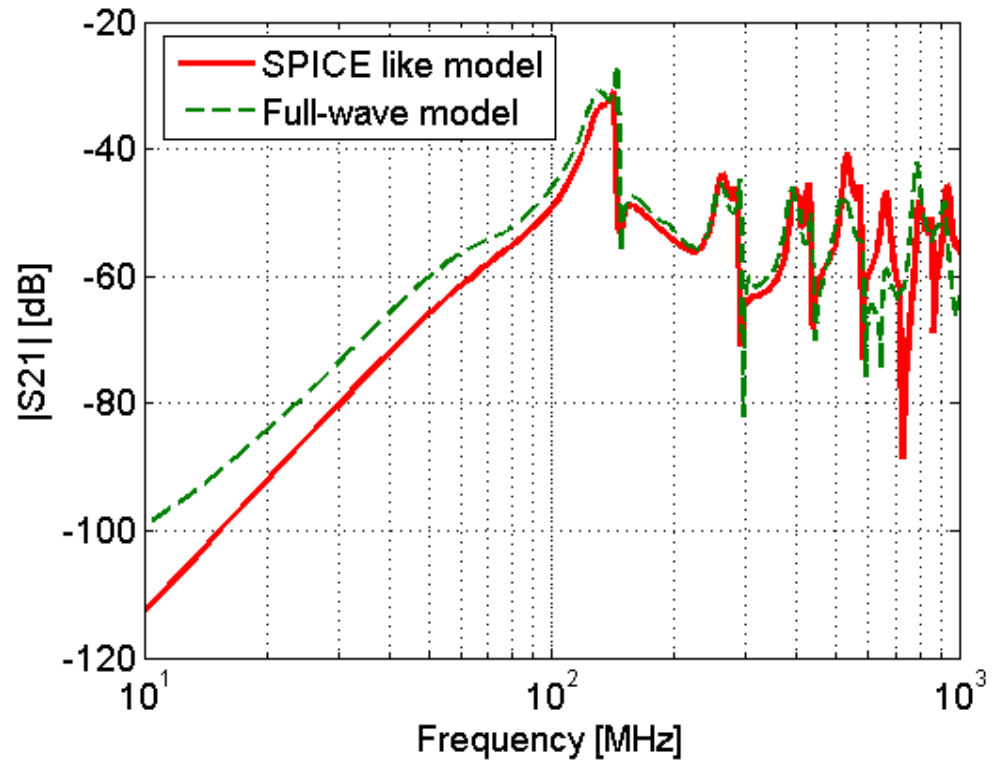
Figure 4.4. Comparison of the measured, simulated (full-wave), and predicted (SPICE) values of $|S_{21}|$ between the cables and the antenna found using the parameters settings for configuration 4 in Table 4.2.
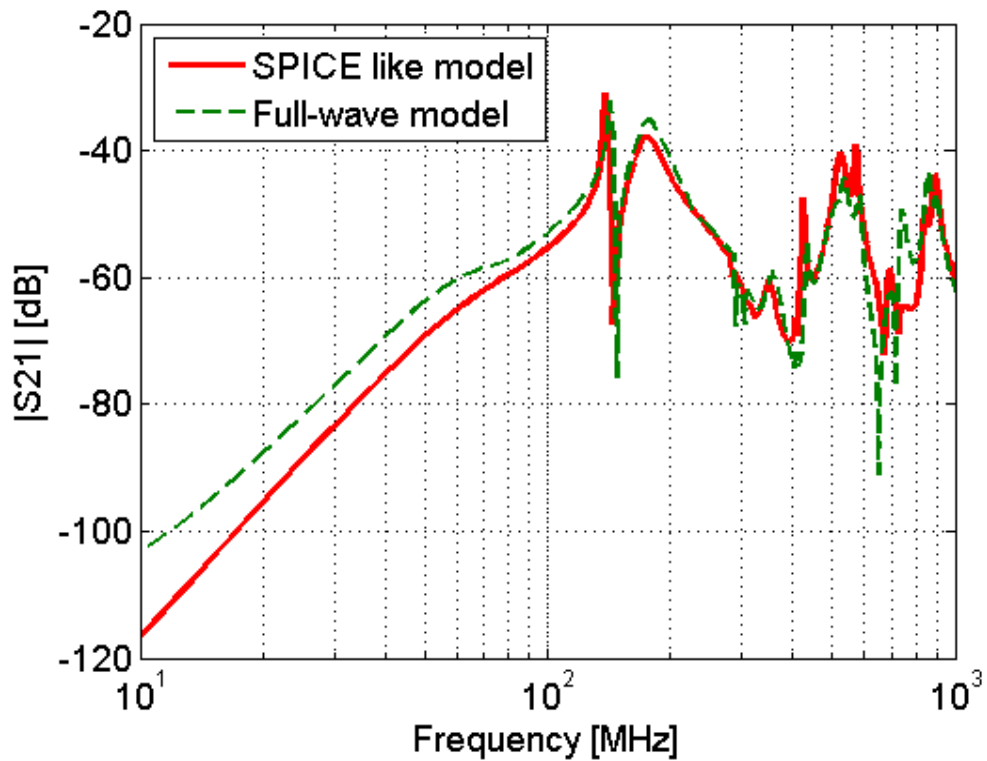
Figure 4.5. Comparison of the measured, simulated (full-wave), and predicted (SPICE) values of $|S_{21}|$ between the cables and the antenna found using the parameters settings for configuration 5 in Table 4.2.
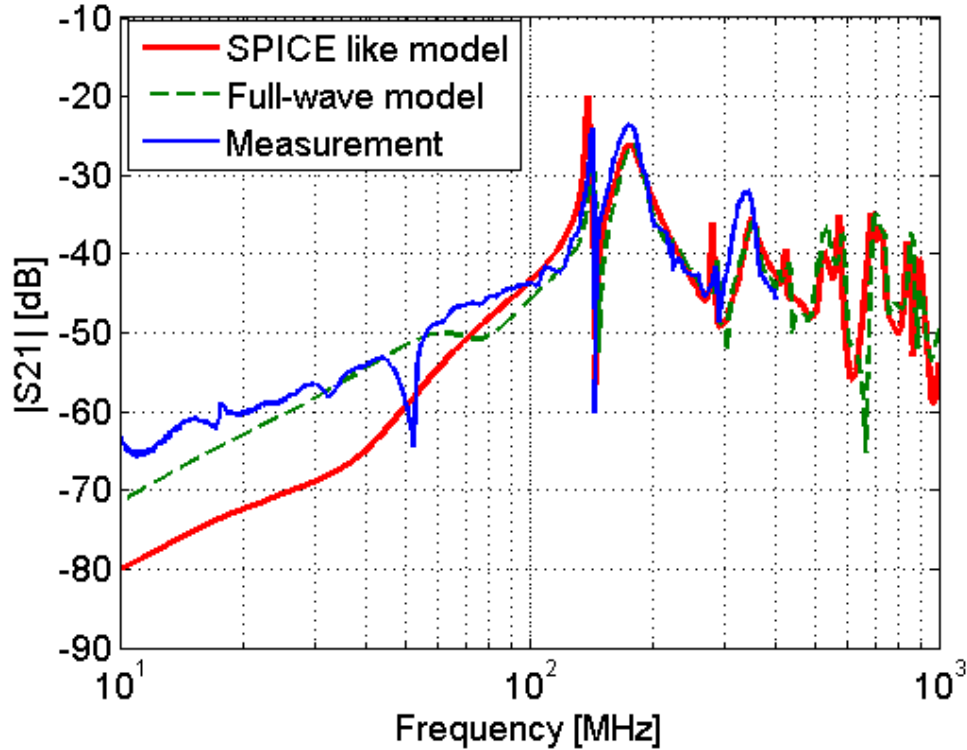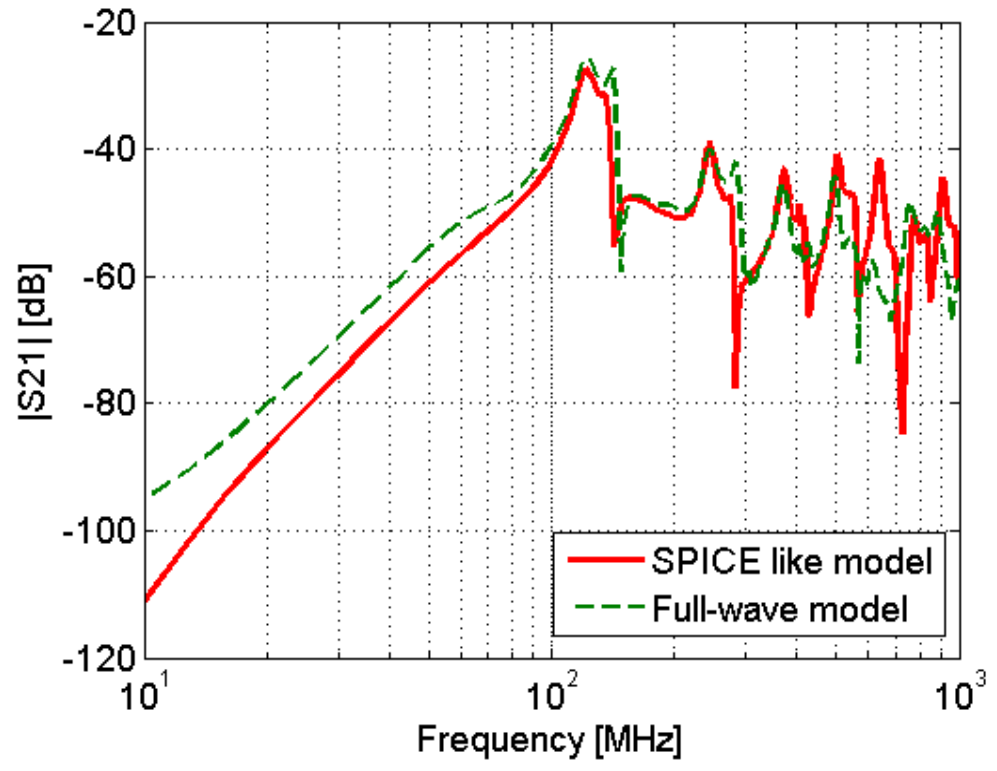
Figure 4.6. Comparison of the measured, simulated (full-wave), and predicted (SPICE) values of $|S_{21}|$ between the cables and the antenna found using the parameters settings for configuration 6 in Table 4.2.
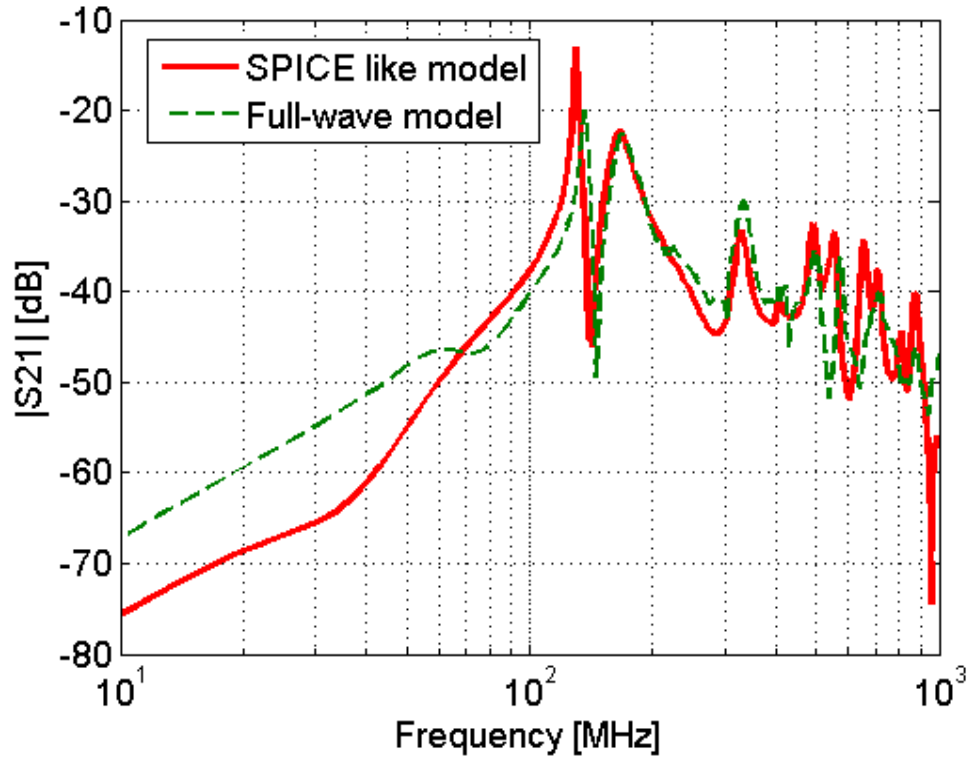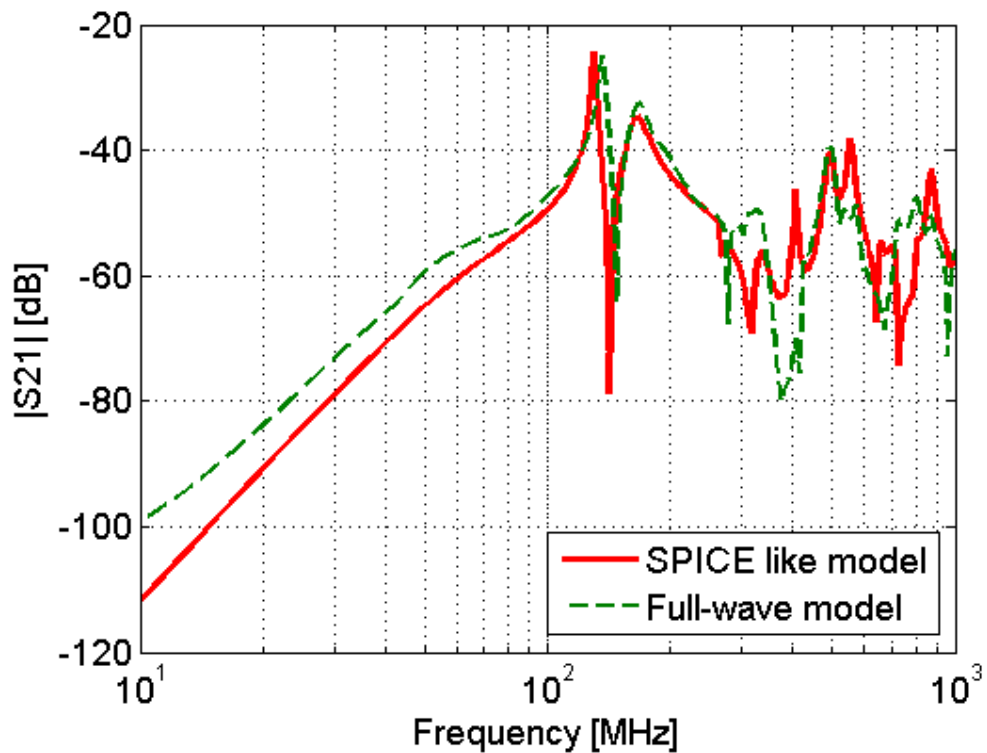
Figure 4.7. Comparison of the measured, simulated (full-wave), and predicted (SPICE) values of $|S_{21}|$ between the cables and the antenna found using the parameters settings for configuration 7 in Table 4.2.

5. DISCUSSION ABOUT CABLE HEIGHT EFFECT

The height of the cables above the ground plane was assumed to be small in Figure 3.2. The horizontal common mode current on the cables is close to its return current on the ground plane, which prevents these currents from contributing significantly to the radiation. When the cable height increases, the contribution of the horizontal currents to the radiation increases, as shown in Figure 5.1 for different cable heights. The horizontal fields will tend to be small when the ground connections are short. When the ground connections are long, the horizontal field may dominate the vertical field. CISPR 25, MIL-STD 461, and DO-160E radiated emission tests require the cables to be 5 cm above the return plane. The equivalent SPICE model is aimed at helping predict worst-case radiated emissions in these real-world tests. The height at which the equivalent SPICE model starts to deviate from full-wave simulation/measurement is well above the height used in the standardized tests.
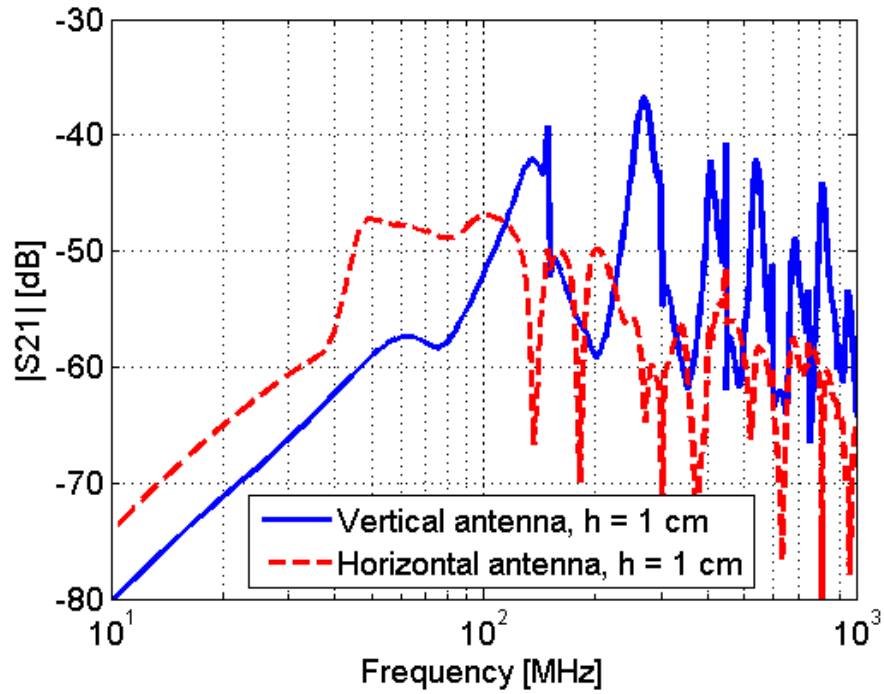
(a)
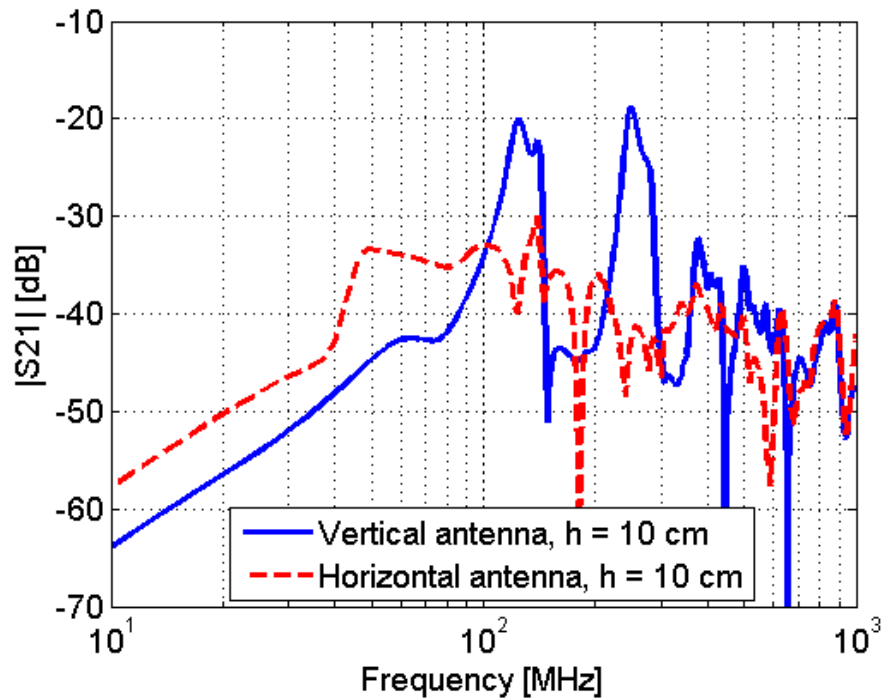
(b)

Figure 5.1. Comparison of radiated emissions from configuration 1 when cables were at different height and when the receiving antenna was horizontal or vertical.
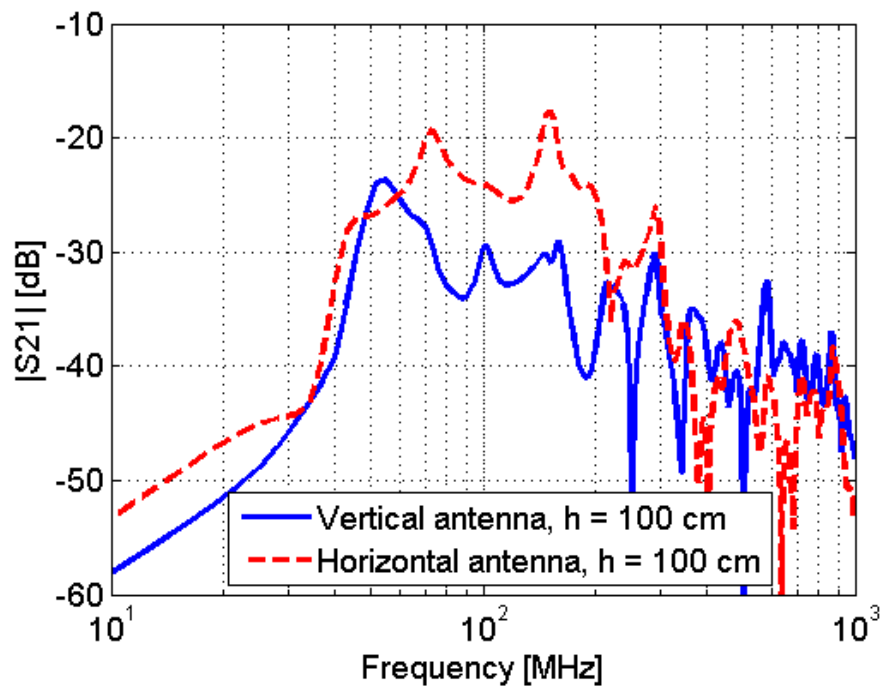
(c)

Figure 5.1. Comparison of radiated emissions from configuration 1 when cables were at different height and when the receiving antenna was horizontal or vertical (cont.).

6. CONCLUSION

An equivalent SPICE model was developed to estimate the radiated emissions from partially shielded cables above a metal plate in component level tests, like those used for CISPR 25, MIL-STD 461, and DO-160. The dominant emissions result from currents in "ground" connections between the cables and the metal return plane for these setups. The currents in the ground connections can be predicted by modeling the cables above the ground plane as transmission lines and by considering the "ground" connections as inductors in series with radiation resistors. The fields from these currents can be approximated using infinitesimal dipoles. Applying the antenna factor of a biconial antenna to the fields gives the observed voltages. Comparisons between predicted and full-wave simulated/measured results demonstrate that this model is able to predict radiated emissions from 60 MHz up to 1 GHz. While the model was developed to predict emissions from shielded wires, it could also be applied to scenarios where the signal wires are unshielded. In that case, the source in Fig. 4 would be placed at the DUT (location x_1) and the entire length of cable from the DUT to load would be treated as a single transmission line. As a SPICE model, it is easy to integrate this model for emissions with existing models of the component circuitry. The models can be applied without the need for sophisticated software or development of sophisticated numerical models. Equally important, since the models are simple, they help provide intuition as to the causes for radiated emissions problem and how they might be fixed.

REFERENCES

[1] CISPR 25: Limits and methods of measurement of radio disturbance characteristics for protection of receivers used on board vehicles, Third edition 2008, IEC.

[2] U.S. Dept. of Defense, "MIL-STD-461D/462D RE102," Jan. 1993.

[3] RTCA DO-160E: Environment conditions and test procedures for airborne equipment, Dec. 2004, RTCA Inc.

[4] D. M. Hockanson, J. L. Drewniak, T. H. Hubing, , T. P. Van Doren, F. Sha, and M. J. Wilhelm, "Investigation of fundamental EMI source mechanisms driving common-mode radiation from printed circuit boards with attached cables," *IEEE Trans. Electromagn. Compat.*, vol. 38, no. 4, pp: 557-566, 1996.

[5] M. Radojicic and G. Costache, "A model to predict radiated emissions from electronic circuits," *in IEEE Int. Symp. Electromagn. Compat.*, Cherry Hill, NJ, 1991, pp. 54 − 57.

[6] D. Schneider, S. Tenbohlen, and W. Kohler, "Pre-compliance test method for radiated emissions of automotive components using scattering parameter transfer function," *in Conf. Rec. 2012 IEEE Europe Conf. EMC*, pp. 1-6.

[7] D. Rinas, J. Jia, A. Zeichner, and S. Frei, "Substituting EMC emission measurement by field and cable scan method using measured transfer function," *Adv. Radio Sci.*, vol. 11, pp. 183-188, 2013.

[8] M. Gonser, C. Keller, J. Hansen, V. Khilkevich, A. Radchenko, D. Pommerenke, and R. Weigel, "Simulation of automotive EMC emission test procedures based on cable bundle measurements," *in Conf. Rec. 2012 IEEE Int. Microwave Symposium Digest*, pp. 1-3.

[9] A. Radchenko, V. Khilkevich, N. Bondarenko, D. Pommerenke, M. Gonser, J. Hansen, C. Keller, "Transfer function method for predicting the emissions in a CISPR-25 test-setup", *IEEE Trans. Electromagn. Compat.*, vol. 56, no. 4, pp: 894-902, 2014.

[10] H. Rebholz and S. Tenbohlen, "A fast radiated emission model for arbitrary cable harness configurations based on measurements and simulations," *in Conf. Rec. 2008 IEEE Int. Conf. EMC*, pp. 1-5.

[11] G. Li, W. Qian, A. Radchenko, G. Hess, R. Hoeckele, P. Jalbert, T. Van Doren, D. Pommerenke and D. Beetner, "Estimating the radiated emissions from cables attached to a switching power supply in a MIL-STD 461 Test," *in IEEE Int. Symp. Electromagn. Compat.*, Denver, CO, 2013, pp. 626-631.

[12] R. Hickey, "Extracting scattering parameters from SPICE," *Application Note, TriQuint Semiconductor*, Nov., 1997.

[13] D. M. Pozar, *Microwave Engineering*, NJ: John Wiley & Sons, Inc., 2011, pp. 54.

[14] C. Hoer and C. Love, "Exact inductance equations for rectangular conductors with applications to more complicated geometries," *J. of Research of the National Bureau of Standards – C. Engr. and Instru*. vol. 69c, no. 2, pp. 127-137, Apr., 1965.

[15] C. A. Balanis, *Antenna Theory: Analysis and Design*, NJ: John Wiley & Sons, Inc., 2005, pp. 155.

[16] D. Schwarzbeck. (2014, Jun. 11). *Inter-Network Talk* [Online]. Available e-mail: support@schwarzbeck.de Message: Biconical Antenna Characterization Environment.

[17] EMCoS Ltd., *EMCoS EMC Studio*, Version 7.0, www.emcos.com.

[18] G. Li, X. Zhao, and K. Huang, "Frequency Dependence of Image Reconstruction of Linear Sampling Method in Electromagnetic Inverse Scattering," *Proc. of Progress In Electromagnetics Research Symp.*, pp. 611-614, March 2010.

[19] G. Li, G. Hess, R. Hoeckele, P. Jalbert, V. Khilkevich, T. Van Doren, D. Pommerenke, and D. Beetner, "Prediction of radiated emissions from cables with multiple connections to a metal plane," in *Asia-Pacific Symp. EMC.*, Taiwan, 2015, accepted for publication.

III. MEASUREMENT-BASED MODELING AND WORST-CASE ESTIMATION OF CROSSTALK INSIDE AN AIRCRAFT CABLE CONNECTOR

Guanghua Li, *Student Member, IEEE*, Gary Hess, Robert Hoeckele, Steve Davidson, Pete Jalbert, Victor Khilkevich, Thomas Van Doren, *Fellow, IEEE*, David Pommerenke, *Senior Member, IEEE*, and Daryl Beetner, *Senior Member, IEEE*

ABSTRACT—Crosstalk within cable bundles can degrade system performance. In aircraft systems that use shielded twisted pairs, the crosstalk occurs primarily in the connector where individual signal wires are not shielded or twisted. In many cases, the parameters which determine crosstalk within the connector are unknown because the connector is closed and wires cannot be easily accessed. Expanding on prior research [14], a methodology for measuring coupling parameters and modeling crosstalk within aircraft cable connectors at low frequencies (< 400 MHz) was developed. The values of mutual inductance and capacitance were extracted from measurements made with a Vector Network Analyzer (VNA). The characteristics of the individual wires were extracted from VNA-measured TDR response. The accuracy of the model was evaluated through comparison of simulated and measured results. Additionally, a closed-form solution was developed to estimate the worst-case envelope of the differential crosstalk. The calculated results match the measured peak values well. This worst-case crosstalk estimate allows effective evaluation of the impact of crosstalk within different connectors. The developed method can be effective for analyzing complex aircraft cable assemblies and connectors without requiring extensive knowledge of the assembly procedure.

Index Terms—Cable bundle, capacitive coupling, crosstalk, inductive coupling, modeling, worst-case crosstalk.

1. INTRODUCTION

Cable bundles in aircraft and automotive systems consist of densely packed power signal wires mixed with high-speed data. The fields generated by one wire couple with another one nearby causing crosstalk. Models for the crosstalk help engineers predict potential issues, which is beneficial for optimizing the system design.

Available crosstalk modeling techniques are based upon multi-conductor transmission line theory [1] with *RLGC* parameters calculated from well-defined cross sections of the multi-conductor transmission lines [2]-[9]. Repeated cross-sectional analysis is applied to include the effect of random or systematic variations of the wire positions [10] [11]. The same approach has been used to analyze the crosstalk in complex aircraft bundles [12] [13], which are made primarily from shielded twisted pairs, with the addition of power wires. The disadvantage of cascading multiple transmission lines is that the cross-section geometry needs to be known in order to construct a wire representation in the cable bundle. In practice, manufacturers might not be able to provide the geometry and its range of variations. The manufacturers generally have little control of the way the cable bundles are assembled into the connectors. It has been shown that most of the coupling between the twisted pairs of the cable bundles occurs at the connectors [14] where the shield has been removed and the wires untwisted. The parameters which determine the crosstalk within the connector are typically unknown and cannot be predicted through modeling because the position of wires within the connector is random and the connector manufacturing technique is not known. Such geometry may be extracted from X-ray scanning, but at high cost for the analysis of only a single cable bundle. Thus, it is not practical to scan every cable bundle for quality control in industrial applications. Another option is dissecting a cable assembly, which would allow the geometry of the cable to be understood. However, this does not lead to an electromagnetically relevant model without transferring the observed imperfections into an equivalent circuit model. In the early stages of design the number of available cables may also be limited, so deconstruction of the connector may not be feasible.

A measurement-based methodology was developed in prior research [14] and extended in this paper to determine the crosstalk parameters within the aircraft cable

connector and to model the crosstalk from a straight wire pair (e.g. power wires against the metal plane below) to shielded twisted pairs within an aircraft cable bundle. The power wires were selected because they do not have shielding layers and carry low-frequency, high-intensity signals which behave as interference sources in the aircraft and automotive systems [6]. The method can be effective for analyzing complex aircraft cable assemblies and connectors without requiring extensive knowledge of the assembly procedure. It only uses transmission lines, mutual capacitance, and mutual inductance to predict the worst-case crosstalk up to 400 MHz.

2. DESCRIPTION OF CABLE BUNDLE

The methodology discussed in this paper was derived from the analysis of a cable bundle shown in Figure 2.1. The cable bundle has 15 wires of 21-AWG size, including: a) one shielded twisted triplet, b) two unshielded single (power) wires, and c) five shielded twisted pairs. The wires of the cable bundle at the near end (or connector end) were inserted into 15 separate pins, which each fit into a connector shell and formed the connector. The connector was then attached to an adaptor made from a Printed Circuit Board (PCB) with fifteen 5 cm long semi-rigid coaxial cables as shown in Figure 2.1 (b). This allows fast and repeatable connection of the wires at the near end [15]. The wires were then separated from each other at some locations along the length of the cable bundle, mimicking the wire routes in an aircraft. At the far end, the wires were not bundled; hence, the far-end crosstalk is not discussed in this paper. The overall cable bundle was enclosed in a 10-cm-long shield directly after the connector shell, as shown in Figure 2.1 (c). The rest of the cable bundle did not share a common shield. The cable bundle was placed on a metal plane, which is analogous to the metal body of an aircraft. The metal plane also provides a current return path for the power wires.

(a)

(b)

(c)
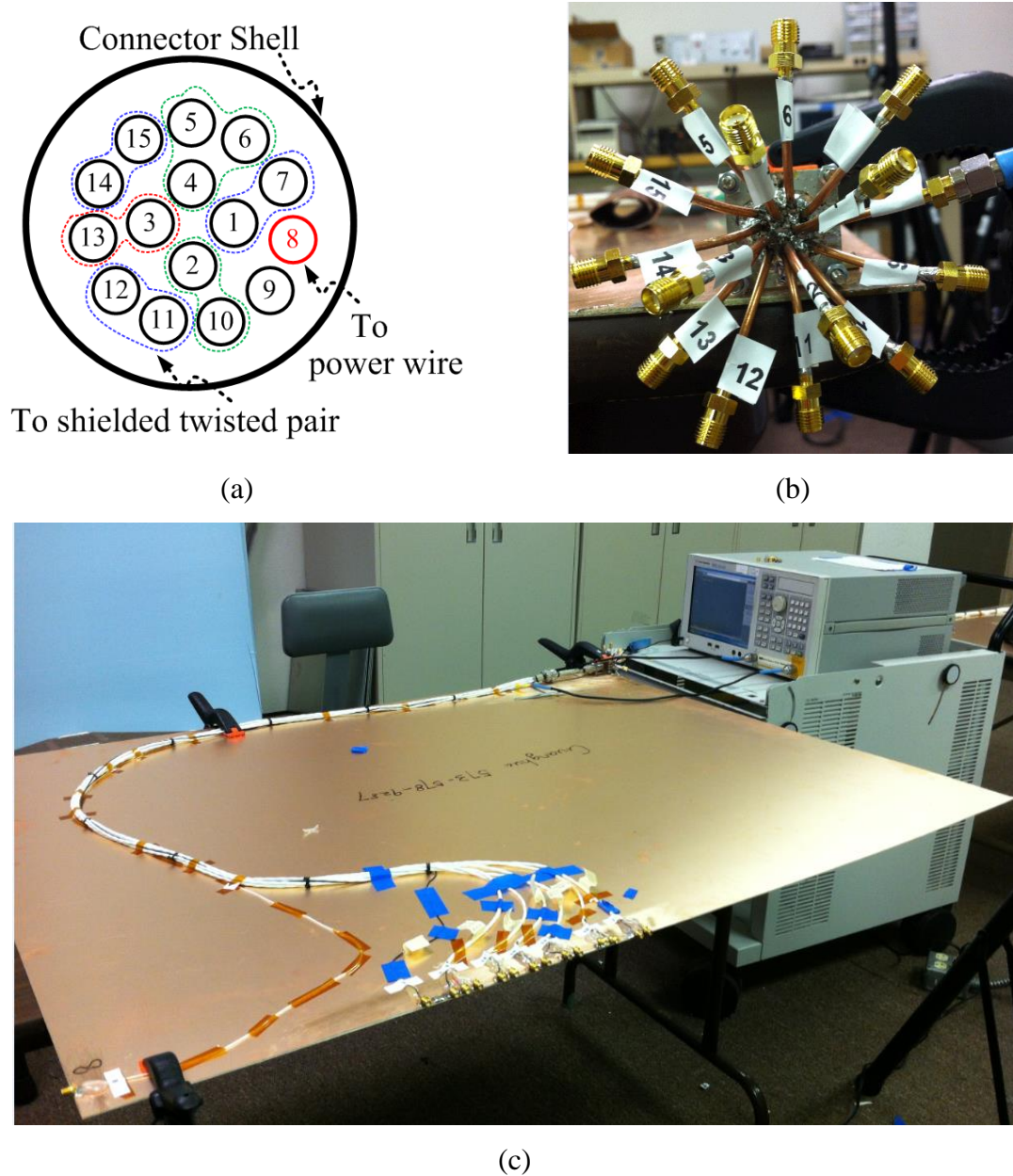
Figure 2.1. Aircraft cable bundle with 15 wires and connector shell above a metal plane, (a) pin sequence in the connector shell, (b) adaptor PCB with 5 cm long semi-rigid coaxial cables, and (c) cable bundle above the metal plane.

The goal was to model the crosstalk from the power wire (against the metal plane as a return path) to the shielded twisted pairs in Figure 2.1(a). The power wire was selected as the starting point because it does not have a shielding layer and may carry high-intensity signals which act as interference sources. The power wire was connected

to pin 8 within the connector shell, as shown in Figure 2.1 (a). One signal wire of the twisted pair was connected to pin 2 of the connector while the other signal wire was connected to pin 10. The single-ended crosstalk was measured at pin 2 or 10 against the shield, while the differential crosstalk was measured between pins 2 and 10.

The fields generated by power wire 8 coupled with the twisted pairs inside the connector shell. Outside the connector shell, power wire 8 and the twisted pairs did not couple because the pairs are shielded. This wire configuration indicates that the coupling from power wire 8 to the twisted pairs occurs primarily within the connector shell and that the coupling inside the cable bundle is negligible.

The crosstalk could potentially be predicted using full-wave simulation tools, but the wire positions within the connector are unknown, as is much of the way that the connector is manufactured. For example, unknown parameters include how far back from the connector pins are the wires untwisted or the shields removed, the electrical properties of the material used to support the pins inside the connector, and the way the shields are connected to the connector. From the outside it is only known that there is a good DC connection between the shields. Therefore, a measurement methodology was developed to directly determine the coupling parameters within the connector, without knowledge of the connector geometry.

3. WIRE-TO-WIRE CROSSTALK MODEL

3.1. CHARACTERISTICS OF WIRES

The radiated emissions are driven by common mode currents on the bare wire, the shield, The cable bundle was placed on the metal plane which formed a transmission line between power wire 8 and the metal plane. Other transmission lines were formed between the signal wires and their shields of the shielded twisted pairs. Both the metal plane and the shield were attached to the connector shell. Measurement ports were defined so that the excitation was between each wire and the connector shell.

The reflection coefficients looking into the ports were measured using a Vector Network Analyzer (VNA), and were then used to generate the time-domain signals to obtain the step response of the transmission lines. The parameters of the transmission lines, such as characteristic impedance and effective dielectric constant, were extracted and listed in Table 3.1. These parameters were validated by comparing the measured and simulated step responses from the cable bundle and its model, respectively. The step response of power wire 8 against the metal plane is shown in Figure 3.1 as an example. It should be mentioned that these comparisons may also be quantified using the Feature Selective Validation (FSV) technique specified in the IEEE standard [16] established in [17], [18]. The discontinuity inside the connector is represented by two self-inductances, $L_{8,8}$ (44 nH) and $L_{10,10}$ (20 nH), as shown in Figure 3.2. The small ripples are caused by different distances along the transmission line between power wire 8 and the metal plane, even though the wire was taped to the metal plane to minimize the distance variation during the measurements.

Table 3.1. Characteristics of Wires against the Metal Plane or its Shield

Pin number	Characteristic impedance Z_0 [Ω]	Effective dielectric constant ε	Transmission line Length [m]
8	65	1.6	2.05
10	35	2.1	2.05
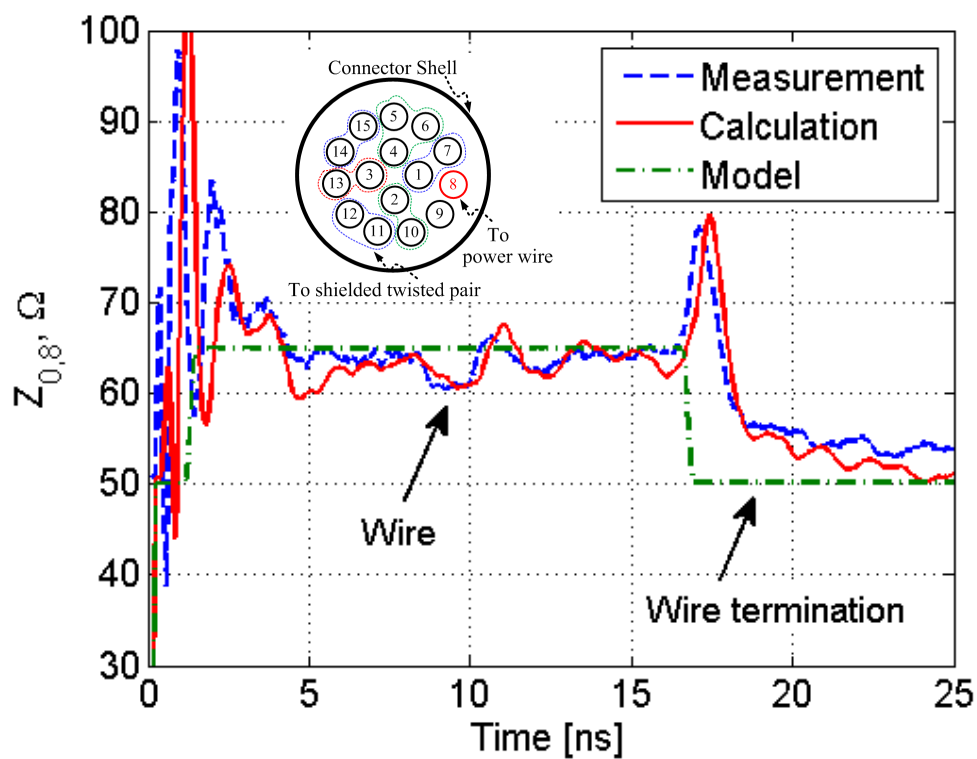
Figure 3.1. Measured, calculated, and modeled characteristics of power wire 8 against the metal plane.
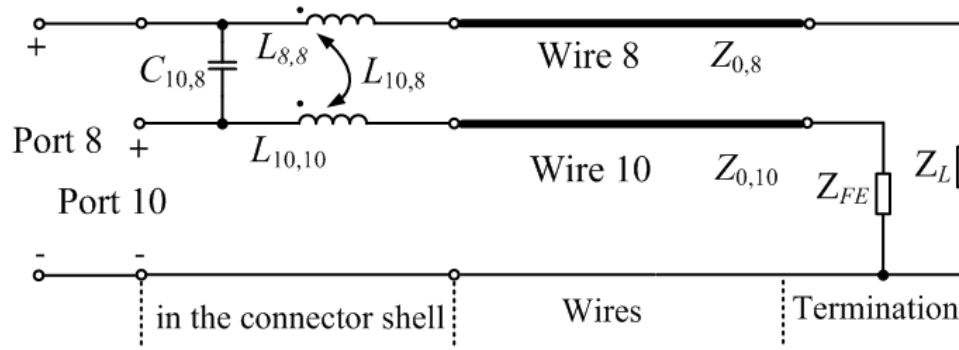
Figure 3.2. Equivalent circuit model of coupling within the connector from power wire 8 to wire 10.

3.2. CHARACTERISTIC OF WIRES

The mutual coupling, as pointed out in Section II, occurs mainly inside the connector. Thus, the wires outside the connector were considered to be uncoupled transmission lines. At frequencies low enough to consider the transmission line as electrically short, the coupling within the conductors can be forced to be either inductively or capacitively dominated by shorting or opening the far ends of the wires, respectively. For the case where the far ends are open-ended, the mutual capacitance, C_{ij}, can be approximated as [14]

$$C_{ij} = \frac{\left|S_{ij,o}(f)\right|}{4\pi f Z_0} \tag{1}$$

where $|S_{ij,o}|$, as shown in Figure 3.3, is the magnitude of the transmission coefficient from one transmission line to another in the frequency range below the first resonance, and Z_0 is the source and load impedance of the measurement device. The mutual inductance, L_{ij}, can be approximated as [14]

$$L_{ij} = \frac{\left|S_{ij,s}(f)\right|Z_0}{4\pi f} \tag{2}$$

where $|S_{ij,S}|$, as shown in Figure 3.4, is the magnitude of the transmission coefficient in the frequency range below the first resonance, when both wires are shorted to ground. The measured mutual inductances and capacitances from power wire 8 to the twisted pairs are listed in Table 3.2. In the table, "weak" means the signal is too weak ($S_{3,8,O}$ or $S_{13,8,O} <$ -100 dB) to be measured. The complete coupling model from power wire 8 to wire 10 is shown in Figure 3.2 as an example, where capacitive coupling is represented with $C_{10,8}$, inductive coupling is represented with a mutual inductance $L_{10,8}$, wires are represented with uncoupled transmission lines, and Z_{FE} and Z_L are terminations of the transmission lines.
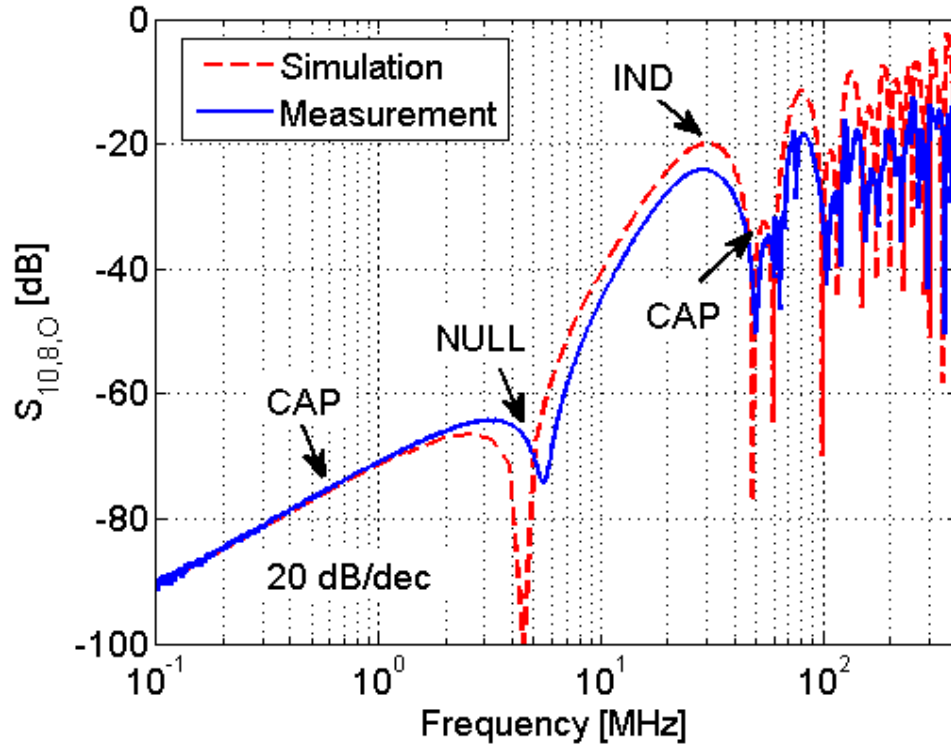
Figure 3.3. Comparison of the measured and predicted values of $|S_{21}|$ between wire 8 and wire 10 when both are terminated with an open, so capacitive coupling dominates at low frequency. The CAP and IND labels indicate the dominant coupling as capacitive and inductive coupling, respectively.
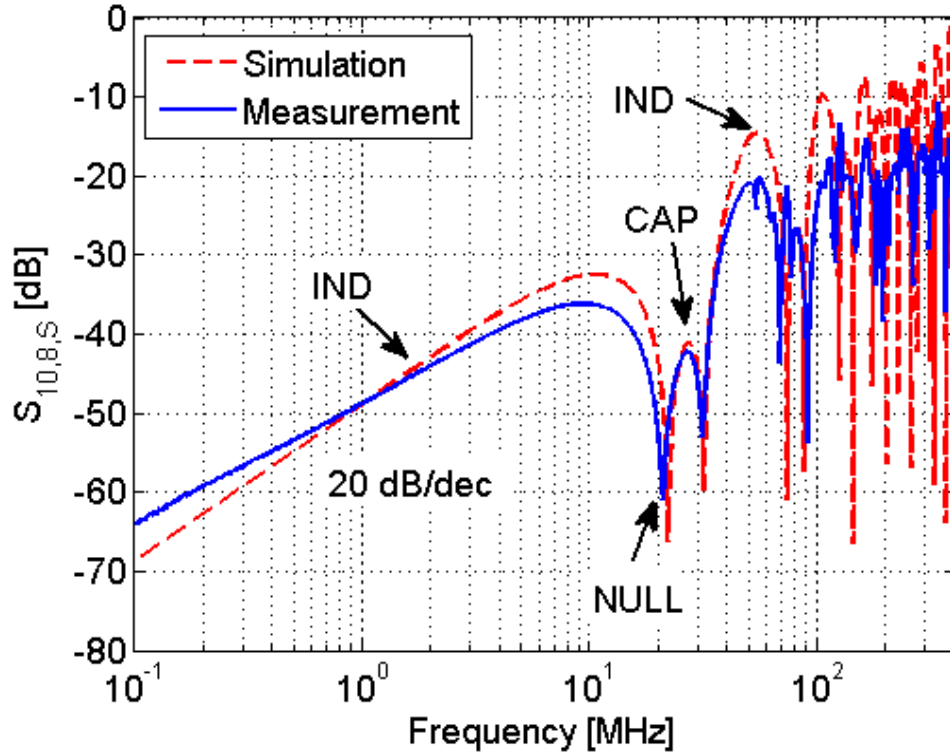
Figure 3.4. Comparison of the measured and predicted values of $|S_{21}|$ between shorted wire 8 and shorted wire 10 when inductive coupling dominates at low frequency.

Table 3.2. Coupling Parameters from Wire 8 to Other Wires

j Pin	k Pin	M_{j8} [nH]	M_{k8} [nH]	C_{j8} [pF]	C_{k8} [pF]
1	7	19.0	17.0	1.1	1.2
2	10	11.6	14.4	0.15	0.45
3	13	12.7	10.7	*Weak*	*Weak*
14	15	12.3	10.8	0.3	0.4
11	12	8.4	11.2	0.02	0.4

3.3. VALIDATION OF WIRE-TO-WIRE CROSSTALK MODEL

The equivalent circuit model was validated against measurements for open and shorted far-end terminations. In the first configuration, the coupling between power wire 8 and wire 10 was investigated, as this case is representative of the coupling from power wire 8 to any of the twisted pairs. The values of $S_{10,8,\,O}$ are shown in Figure 3.3. At low frequency, the wires attached to the connector were electrically short, thus a high impedance was seen. Capacitive coupling was shown to dominate over inductive coupling, as indicated from (1) where the slope of $|\,S_{10,8,\,O}\,|$ is +20 dB/dec. The portion of the curves where capacitive coupling dominates was labeled as CAP in the figure.

As frequency increased, the wires became electrically long and the open termination ($Z_L = Z_{FE} = \infty$) was transformed to a smaller input impedance seen when looking from the connector into the cable. The current in power wire 8 induced a voltage drop across the twisted pair through mutual inductance. Simultaneously, the current source from the mutual capacitance still coupled energy from power wire 8 to wire 10. The induced voltage from the current source at port 10 cancelled the effect of the induced voltage from inductive coupling, which resulted in a null in $|S_{10,8,\,O}|$ between 5 and 6 MHz in Figure 3.3.

As the frequency increased further, the wires became a quarter-wavelength long, and the open terminations Z_L and Z_{FE} were transformed to short terminations when looking into the transmission line from the connector. The dominant coupling mechanism became inductive coupling, which was labeled as IND in the figure. The effective dielectric constant of the material around the wires was about 2.1 and the wires were about 2 m long which placed the quarter-wavelength frequency at approximately 25 MHz. The first peak in $|S_{10,8,\,O}|$ followed the first null and occurred at 28 MHz, which is close to this expected frequency.

When the wires became a half-wavelength long, capacitive coupling again became the dominant coupling mechanism. A half wavelength transformation should have occurred at approximately 50 MHz, returning the load conditions to open ($Z_L = Z_{FE} = \infty$). The second peak of $|S_{10,8,\,O}|$ (attributed to capacitive coupling) occurred at 54 MHz, which closely matched the prediction.

The impedance looking into the cables attached to the connector was transformed from an open to a short and back every quarter wavelength. The dominant coupling mechanism in the induced signal switched between capacitive and inductive, causing the peak levels above 54 MHz to alternate between high and low levels. So long as the connector was electrically small and the loss in the cable was ignored, the inductive and capacitive coupling increased at 20 dB/dec, as shown in Figure 3.3.

Similar observations were made for other configurations. A comparison of the measured and predicted values of $|S_{10,8,S}|$ is shown in Figure 3.4. In each case, the measured and predicted values matched within 7 dB up to about 400 MHz.

4. WIRE-TO-TWISTED WIRE PAIR CROSSTALK MODEL

4.1. CHARACTERISTICS OF TWISTED WIRE PAIR

The twisted pairs were characterized with single-ended, 2-port VNA measurement by terminating all unmeasured ports in Figure 4.2 (a) with 50 Ω loads and measuring two ports at a time. The 2-port S-parameters were then used to generate time-domain signals to obtain the differential-mode (DM) and common-mode (CM) characteristics, including impedance and effective dielectric constant. The parameters of the twisted pairs are summarized in Table 4.1. The measured, calculated, and modeled DM and CM characteristic impedances are shown in Figure 4.1. The far-end terminations of the twisted pairs were formed by two 50 Ω resistors, each between the signal conductors and the shield. Therefore, 100 Ω DM impedance and 25 Ω CM impedances were observed after 20 ns, which is the electrical length of the cable. Compared to the characteristic impedance shown in Figure 3.1, the DM and CM characteristic impedances had smaller variations along the propagation direction. This reduced variation occurs because the cross-section of the twisted pairs had less translational variation than the single-ended power wire 8.

Table 4.1. Parameters of the Twisted Wire Pairs

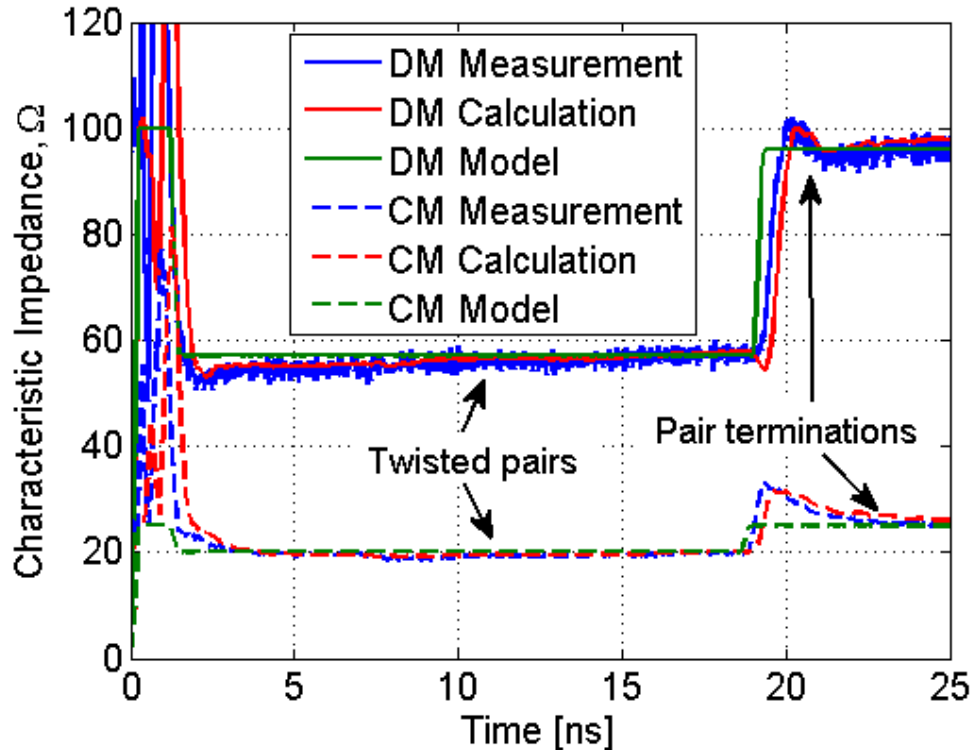| Parameters	Values	Parameters	Values
Z_{DM}	57 Ω	Z_{CM}	20 Ω
ε_{DM}	2.0	ε_{CM}	1.9
Length	2.05 m	Length	2.05 m

Figure 4.1. Comparison of modeled and measured differential- and common-mode characteristic impedance for the twisted wire pair.

4.2. DIFFERENTIAL COUPLING MODELING AND VALIDATION

A differential coupling model was created to model the coupling from power wire 8 (aggressor) to other victim wires, as shown in Figure 4.2 (b). In the model, weak coupling was assumed; i.e., both the coupling from the victim back to the aggressor and the coupling among the victim wires were neglected. The capacitive coupling is represented as mutual capacitance, while the inductive coupling is represented as a current controlled voltage source. The values of the mutual inductance and capacitance were obtained from the wire-to-wire coupling measurement and listed in Table II. The twisted pair was modeled as two coupled transmission lines with DM and CM impedances as characterized above. The far end of the aggressor was connected to ZL and the far ends of the victims were each connected to Z_{FE}. A source port with an impedance of 50 Ω was assigned to power wire 8 at the connector and numbered as port 8. Ten receiving ports were assigned to the five twisted pairs $\{j, k\}$. Each port had a load

impedance of 50 Ω. The coupling from the power wire to the differential mode of the

twisted pairs is expressed as

$$S_{(j,k),8} = S_{j8} - S_{k8} \tag{3}$$

(a)

(b)
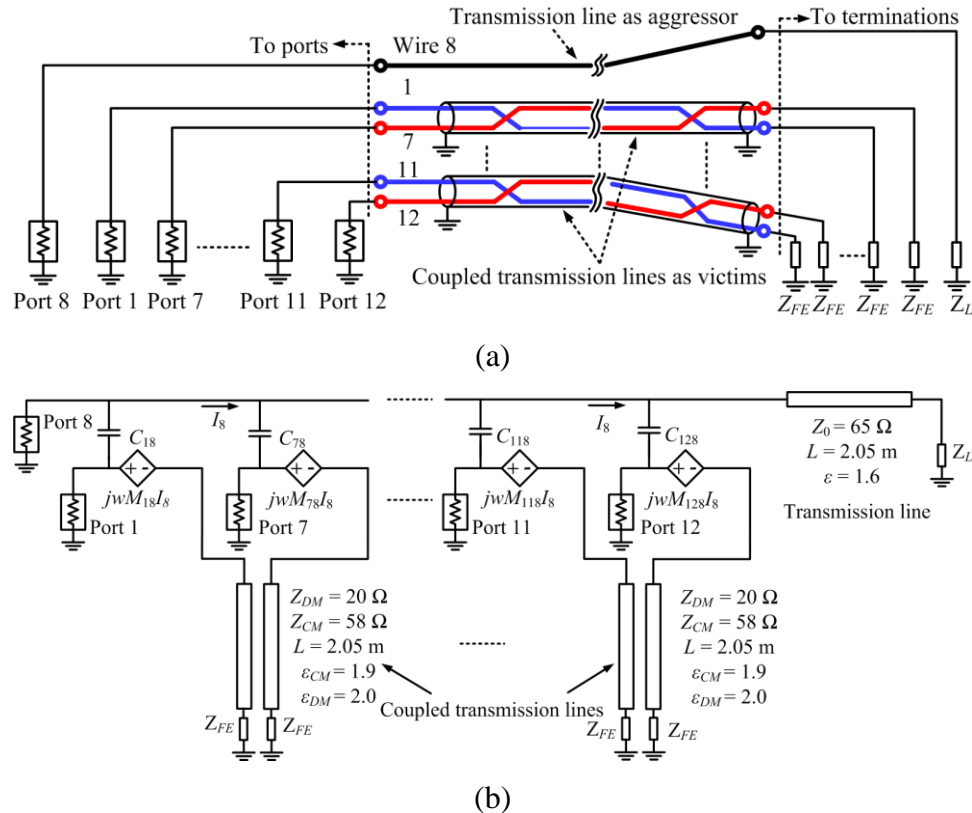
Figure 4.2. Differential coupling between aggressor wire 8 and twisted wire pairs with (subfigure a) a schematic of the measurement setup and (subfigure b) an equivalent circuit model of the differential coupling. A transmission line in (b) was used to represent power wire 8 in (a), while coupled transmission lines in (b) were used to represent the twisted pairs in (a). The capacitances were used to represent capacitive coupling, while the current controlled voltage sources were used to represent inductive coupling.

A set of comparisons between measured and modeled differential coupling was

performed. Two of the comparisons are shown in Figure 4.3 and Figure 4.4 as

representative examples. The modeled differential coupling matches the measured

coupling within 5 dB. Additional comparison with the differential crosstalk from an aggressor to a 1.9 m long unshielded twisted pair around 1 MHz in [19] further validates that the coupling within the connector shell is dominant over the crosstalk along the cable in certain cases.

Figure 4.3. Comparison of measured and simulated inductive differential coupling from wire 8 to pair {2, 10}. The far ends of the transmission lines are shorted to ground.

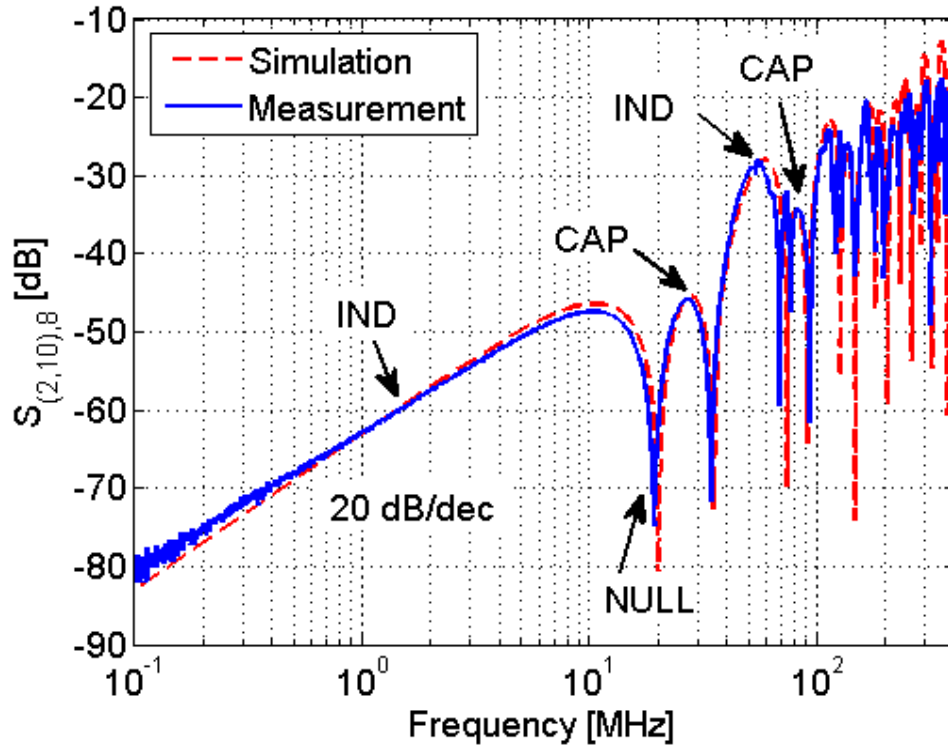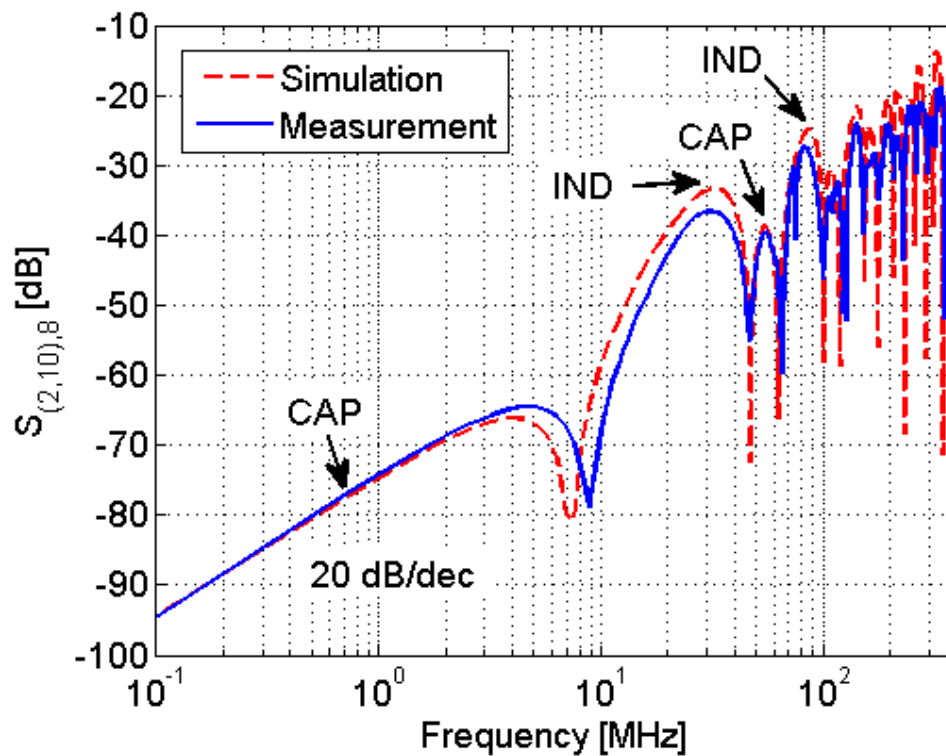Figure 4.4. Comparison of measured and simulated capacitive differential coupling from wire 8 to pair {2, 10}. The far ends of the transmission lines are open.

5. WORST-CASE CROSSTALK ESTIMATION

In Sections III and IV, the TDR response was used to extract the characteristics associated with each wire. These values were critical for the equivalent circuit model to accurately predict the crosstalk from the aggressor wire to the victim wires at all frequencies. The detailed prediction of crosstalk included estimations of the frequency at which the first null of $|S_{21}|$ occurs, the frequency at which the inductive coupling is dominant in the induced signal, the frequency at which the capacitive coupling is dominant in the induced signal, and the frequency interval between two neighboring peaks. While this information might be useful in many applications, the engineer is only interested in the worst-case crosstalk. A closed-form solution which predicts the worst-case crosstalk can be obtained by ignoring the wire characteristics that were part of the models in Figure 3.2 and Figure 4.2.

5.1. DERIVATION OF WORST-CASE DIFFERENTIAL CROSSTALK

An equivalent circuit model shown in Figure 5.1 was used to derive the solution to the worst-case crosstalk when inductive coupling was dominant. Z_s represents the source impedance, while Z_j and Z_k represent the load impedance. The single wire (power wire) is represented by the aggressor transmission line in the model, while the twisted pairs are represented by the victim coupled transmission lines. Mutual capacitive coupling between the aggressor and victim lines was ignored because the strongest capacitive coupling and the strongest inductive coupling do not occur under the same conditions, as indicated in Figure 4.3 and Figure 4.4.

The schematic shown in Figure 5.1 was transformed with a Y circuit used for the coupled transmission lines (victim) and is shown in Figure 5.2. The parameters of a lossless transmission line, Z_{ii}, Z_{kk}, and Z_L, are purely reactive when the transmission line is shorted to ground. The aggressor transmission line parameter Z_{ii} is also purely reactive.
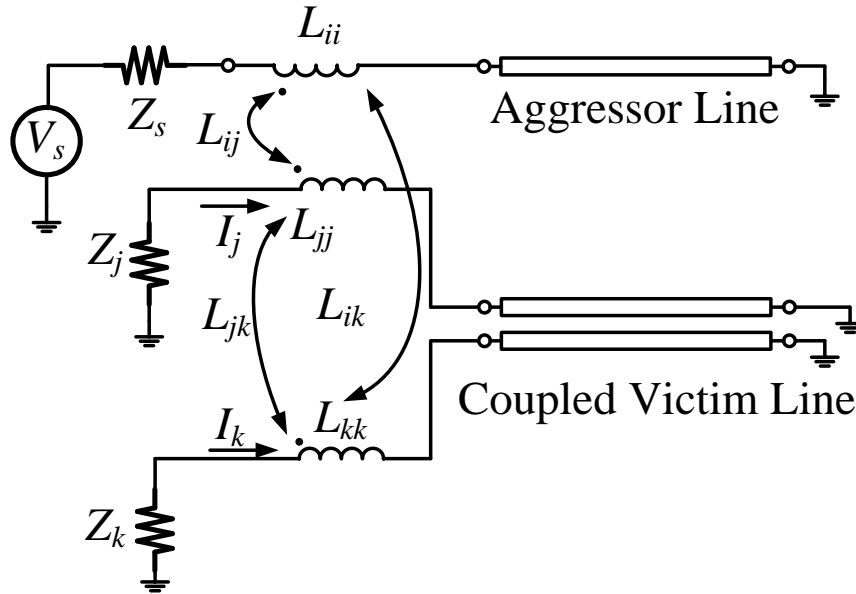
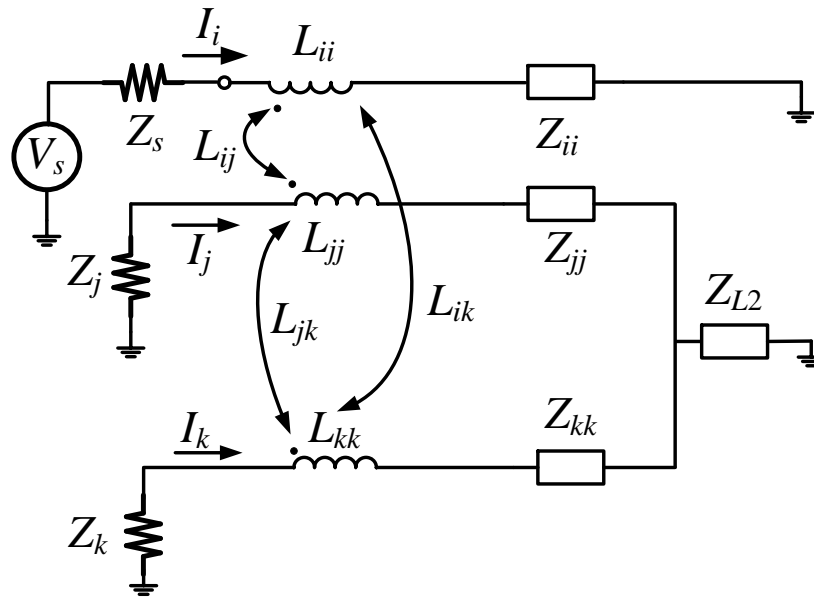Figure 5.1. Schematic for deriving the worst-case inductive differential crosstalk.

Figure 5.2. Transformed schematic from Figure 5.1 for deriving the worst-case inductive differential crosstalk.

Applying KVL for each current I_i, I_j, and I_k in Figure 5.2 gives

$$\begin{cases} (Z_s + Z_{ii} + j\omega L_{ii})I_i + j\omega L_{ij}I_j + j\omega L_{ik}I_k = V_s \\ (Z_j + j\omega L_{jj})I_j + j\omega L_{jk}I_k + Z_{jj}I_j + Z_{L2}(I_j + I_k) = -j\omega L_{ij}I_i \\ (Z_k + j\omega L_{kk})I_k + j\omega L_{jk}I_j + Z_{kk}I_k + Z_{L2}(I_j + I_k) = -j\omega L_{ik}I_i \end{cases} \tag{4}$$

For weakly coupled wires, the induced voltages from the victim to the aggressor is assumed to be zero; that is, $j\omega L_{ij}I_j = j\omega L_{ik}I_k = 0$. The DM and CM currents, I_j-I_k and I_j+I_k, can be calculated from the following equations:

$$\begin{bmatrix} a & b \\ b & d \end{bmatrix} \cdot \begin{bmatrix} I_j - I_k \\ I_j + I_k \end{bmatrix} = \begin{bmatrix} j\omega(L_{ik} - L_{ij})I_i \\ -j\omega(L_{ik} + L_{ij})I_i \end{bmatrix} \tag{5}$$

where

$$Z_j = Z_k,$$

$$a = Z_j + Z_{jj} + j\omega L_{jj} - j\omega L_{jk} + \frac{j\omega\Delta_L + \Delta_Z}{2},$$

$$b = -\frac{j\omega\Delta_L + \Delta_Z}{2},$$

$$d = Z_j + 2Z_{L2} + Z_{jj} + j\omega L_{jk} + j\omega L_{jj} + \frac{j\omega\Delta_L + \Delta_Z}{2},$$

$$\Delta_L = L_{kk} - L_{jj},$$

and

$$\Delta_Z = Z_{kk} - Z_{jj}$$

When the series combination of $j\omega L_{ii}$ and Z_{ii} in Figure 5.2 is zero, the source current I_i in the aggressor transmission line is at a maximum,

$$I_{i,\mathrm{max}} = \left. \frac{V_s}{Z_s} \right|_{j\omega L_{ii} + Z_{ii} = 0} \tag{6}$$

When $L_{jj} = L_{kk}$ and $Z_{jj} = Z_{kk}$ in Figure 5.2, there is no mode conversion and the imaginary part of a in (5) is zero,

$$a = \left. Z_j \right|_{Z_{jj} + j\omega L_{jj} - j\omega L_{jk} = 0} \text{, if } \Delta_L = \Delta_Z = 0 \tag{7}$$

The DM current I_j-I_k in the victim loop is also at a maximum. The DM voltage across Z_j and Z_k can then be calculated as

$$V_{DM} = j\omega (L_{ik} - L_{ij}) \frac{V_s}{Z_s} \tag{8}$$

The DM voltage increases with a slope of 20 dB/dec, until losses start decreasing the loop currents, which is not discussed here.

Similarly, when capacitive coupling is dominant, the DM voltage across Y_j and Y_k can be derived from the model in Figure 5.3.

$$\begin{bmatrix} a & b \\ -b & d \end{bmatrix} \cdot \begin{bmatrix} V_j - V_k \\ V_j + V_k \end{bmatrix} = \begin{bmatrix} -j\omega V_s (C_{ij} - C_{ik}) \\ j\omega V_s (C_{ij} + C_{ik}) \end{bmatrix} \tag{9}$$

where

$$Y_j = Y_k,$$

$$a = -Y_j - 2Y_{jk} - j\omega C_{ij} - Y_{ii} + \frac{j\omega \Delta_C + \Delta_Y}{2},$$

$$b = -\frac{j\omega\Delta_C + \Delta_Y}{2},$$

$$d = Y_j + j\omega C_{ij} + Y_{jj} - \frac{j\omega\Delta_C + \Delta_Y}{2},$$

$$\Delta_C = C_{ij} - C_{ik},$$

and

$$\Delta_Y = Y_{jj} - Y_{kk}.$$

When the imaginary parts of a and d in (9) are zero, a solution to the worst-case crosstalk can be calculated as

$$\begin{bmatrix} -Y_j & -\dfrac{j\omega\Delta_C}{2} \\ \dfrac{j\omega\Delta_C}{2} & Y_j \end{bmatrix}\begin{bmatrix} V_j - V_k \\ V_j + V_k \end{bmatrix} = \begin{bmatrix} -j\omega V_s(C_{ij} - C_{ik}) \\ j\omega V_s(C_{ij} + C_{ik}) \end{bmatrix} \tag{10}$$

It can be inferred from (8) and (10) that the induced worst-case DM voltage depends on the difference of two mutual inductances or mutual capacitances, and that the slope of the induced voltage is 20 dB/dec.
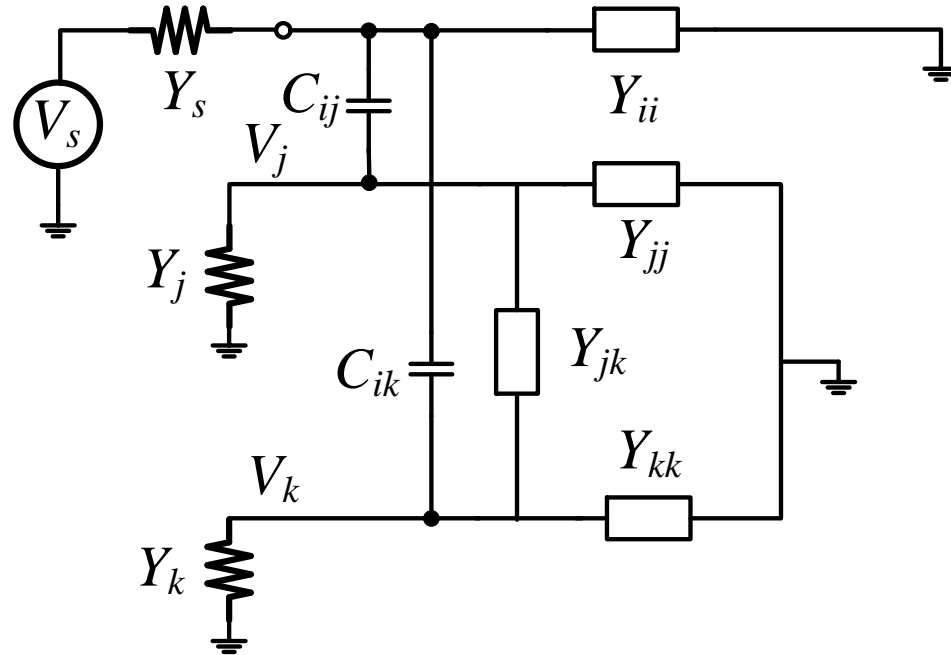
Figure 5.3. Equivalent circuit model for developing the worst-case capacitive differential crosstalk.

5.2. VALIDATION OF WORST-CASE DIFFERENTIAL CROSSTALK

The worst-case crosstalk estimate was validated against measurements using inductive-dominant coupling and capacitive-dominant coupling configurations. As shown in Figure 4.2, the source and load impedances are 50 Ω at the near ends of the transmission lines and the far ends are shorted to ground. For the induced voltage configuration, the maximum inductive coupling is stronger than the maximum capacitive coupling. The estimated envelope using (8) captured the measured peak values of crosstalk for the twisted wire pair {2, 10}, as shown in Figure 5.4. The estimated worst-case crosstalk and measured peak values for other pairs also followed this pattern.

Figure 5.4. Predicted envelope of crosstalk for inductive differential coupling using the model shown in Figure 4.2. The victim is the twisted wire pair {2, 10}. The near-end impedance is 50 Ω.

For the capacitively dominant coupling configuration, the far ends of the transmission lines were terminated with an open, while the near-end source and load impedances were set to a high impedance of 300 Ω. This larger near-end impedance led to smaller aggressor currents in (5), and consequently less inductively induced DM voltage in (7). The capacitively induced voltage in (8) increased, since the admittance Y_j became smaller while the DM source $-j\omega V_s (C_{ij} - C_{ik})$ remained the same. In order to compare the estimated crosstalk with the measured crosstalk, the measurement was renormalized to 300 Ω from the 50 Ω used previously by the VNA. The estimated maximum crosstalk envelope using (10) captured the measured peak values for the twisted wire pair {2, 10} within 6 dB, as shown in Figure 5.5.
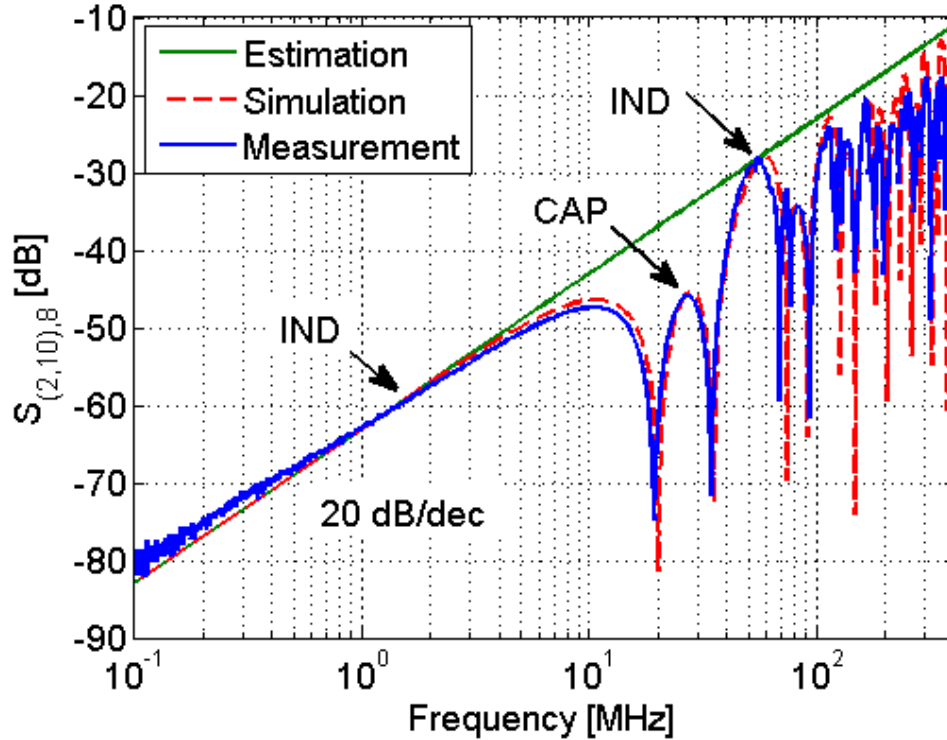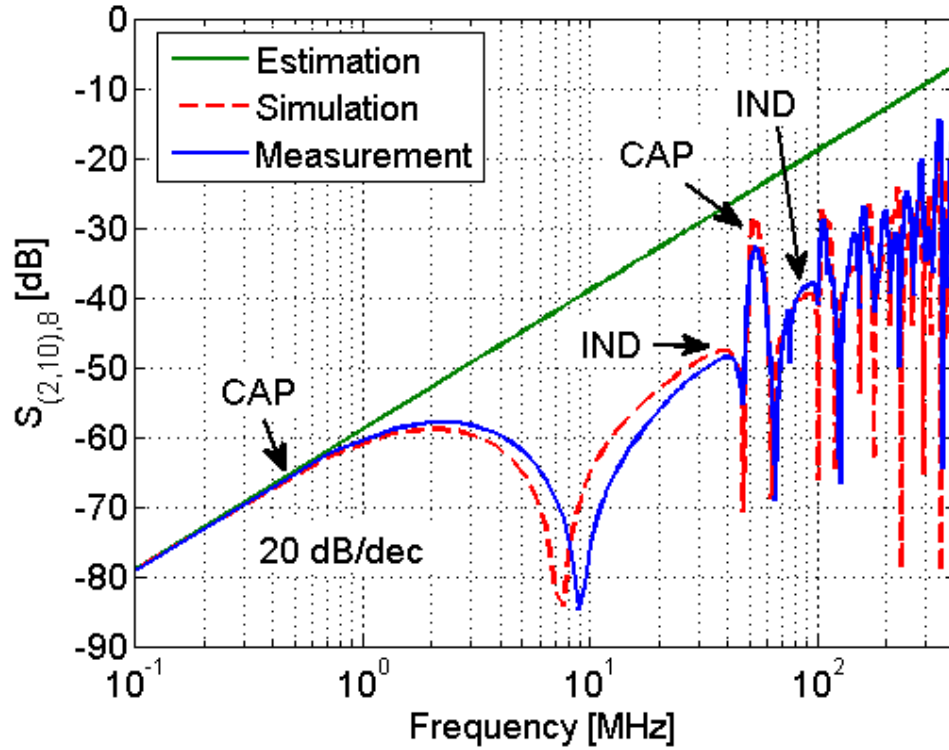
Figure 5.5. Predicted envelope of crosstalk for capacitive differential coupling using the model in Figure 4.2. The victim is the twisted wire pair {2, 10}. The near-end impedance is 300 Ω.

6. CONCLUSION

An experimental methodology based on VNA measurements was developed in order to determine the coupling parameters within a cable bundle, and the characteristic impedance and effective dielectric constant of the wires. To predict the single-ended and differential crosstalk between the wires, an equivalent circuit model was created. The model was then validated against actual measurement results. A closed-form expression for estimating the worst-case crosstalk in the cable bundle, when the coupling mainly occurs inside the connector shell, was also derived and evaluated. The closed-form expression is shown to be reasonably accurate as maximum crosstalk estimates are generally within 6 dB of the peak crosstalk measured from this cable bundle. These results indicate this measurement-based method can be effective for analyzing complex aircraft cable assemblies and connectors without requiring extensive knowledge of the assembly procedure.

REFERENCES

[1]   C. R. Paul, Analysis of Multiconductor Transmission Lines, 1994: Wiley.

[2]   C. R. Paul and J. W. McKnight, "Prediction of crosstalk involving twisted pairs of wires—Part I: A transmission-line model for twisted-wire pairs", *IEEE Trans. Electromagn. Compat.*, vol. EMC-21, no.2, pp. 92-105, 1979.

[3]   C. R. Paul and J. W. McKnight, "Prediction of crosstalk involving twisted pairs of wires—Part II: A simplified low-frequency prediction model", *IEEE Trans. Electromagn. Compat.*, vol. EMC-21, no. 2, pp. 105-114, 1979.

[4]   C. R. Paul and A. E. Feather, "Computation of the transmission line inductance and capacitance matrices from the generalized capacitance matrix," *IEEE Trans. Electromagn. Compat.*, vol. EMC-18, no. 4, pp. 175-183, 1976.

[5]   A. Roy, S. Ghosh, and A. Chakrabarty, "Simple crosstalk model of three wires to predict near end and far end crosstalk in an EMI/EMC environment to facilitate EMI/EMC modeling," *Progress In Electromagnetics Research*, vol. 8, pp. 43-58, 2008.

[6]   Z., Li, Z. Shao, J. Ding, Z. Niu, and C. Gu, "Extension of the "Equivalent Cable Bundle Method" for Modeling Crosstalk of Complex Cable Bundles," *IEEE Trans. Electromag. Compat.,* vol. 53, no. 4, pp. 1040-1049, 2011.

[7]   D. Bellan and S. A. Pignari, "Efficient estimation of crosstalk statistics in random wire bundles with lacing cords," *IEEE Trans. Electromag. Compat.* vol. 53, no. 1, pp. 209-218, 2011.

[8]   Z., Li, L. Liu, J. Ding, M. Cao, Z. Niu, and C. Gu, "A new simplification scheme for crosstalk prediction of complex cable bundles within a cylindrical cavity," *IEEE Trans. Electromag. Compat.*, vol. 54, no. 4, pp. 940-943, 2012.

[9]   C. Jullien, P. Besnier, M. Dunand, and I. Junqua, "Advanced modeling of crosstalk between an unshielded twisted pair cable and an unshielded wire above a ground plane," *IEEE Trans. Electromag. Compat.*, vol. 55, no. 1, pp. 183-194, 2013.

[10]   S. Sun, G. Liu, J. L. Drewniak, and D. J. Pommerenke, "Hand-assembled cable bundle modeling for crosstalk and common-mode radiation prediction," *IEEE Trans. Electromag. Compat.*, vol. 49, no. 3, pp. 708-718, 2007.

[11]   M. Wu, D. G. Beetner, T. H. Hubing, H. Ke, and S. Sun, "Statistical prediction of reasonable worst-case crosstalk in cable bundles," *IEEE Trans. Electromagn. Compat.*, vol. 51, no. 3, pp. 842-851, 2009.

[12] C. Jullien, P. Besnier, M. Dunand, and I. Junqua, "Crosstalk analysis in complex aeronautical bundle," *Proc. of the 2013 International Symp. On Electromag. Compat. (EMC Europe 2013),* Brugge, Belgium, Sept. 2-6, 2013, pp. 253–258.

[13] S. Arianos, M. Francavilla, M. Righero, F. Vipiana, P. Savi, S. Bertuol, M. Ridel, J. Parmantier, L. Pisu, M. Bozzetti, and G. Vecchi, "Evaluation of the modeling of an EM illumination on an aircraft cable harness," *IEEE Trans. Electromag. Compat.*, vol. 56, no. 4, pp. 844-853, 2014.

[14] G. Li, J. He, G. Hess, R. Hoeckele, P. Jalbert, T. Van Doren, and D. Beetner, "Measurement-based models for crosstalk within a connector shell," *in IEEE Int. Symp. Electromag. Compat.*, Rayleigh, NC, 2014, pp. 283-288.

[15] M. Gonser, C. Keller, J. Hansen, and R. Weigel, "Development of a multiport test bench and systematic measurements of cable bundles for automotive EMC tests," *Advances in Radio Science*, vol. 8, no. 13, pp. 203-209, 2010.

[16] Standard for Validation of Computational Electromagnetics Computer Modeling and Simulation – Part 1, 2, IEEE Standard P1597, 2008.

[17] A.P. Duffy, A.J.M. Martin, A Orlandi, G Antonini, T.M. Benson, and M.S. Woolfson, "Feature Selective Validation (FSV) for validation of computational electromagnetics (CEM). Part I – The FSV method", *IEEE Trans. Electromagn. Compat.*, vol. 48, no. 3, pp. 449–459, 2006.

[18] A. Orlandi, A.P. Duffy, B. Archambeault, G. Antonini, D. E. Coleby, and S. Connor "Feature Selective Validation (FSV) for validation of computational electromagnetics (CEM). Part II – Assessment of FSV performance", *IEEE Trans. Electromagn. Compat.*, vol. 48, no. 3, pp. 460-467, 2006.

[19] G. Spadacini and S. A. Pignari, "Impact of common-to-differential mode conversion on crosstalk in balanced twisted pairs," *in IEEE Int. Symp.Electromag. Compat.*, Portland, USA, 2006, pp. 145-150.

[20] G. Li, V. Prabhala, A. Saxena, Q. Wang, P. Maheshwari, and D. Pommerenke, "A methodology to generate a time-varying adjustable wave impedance inside a TEM cell," *in IEEE Int. Symp. EMC*, Rayleigh, NC, 2014, pp. 894-898.

[21] N. Bondarenko, Z. Li, B. Xu, G. Li, T. Van Doren, D. Loken, P. Berger, and D. Beetner, "A measurement-based model of the electromagnetic emissions from a power inverter," *IEEE Trans. Power Electron.*, vol. 30, no. 10, pp. 5522-5531, 2015.

[22] X. Jiao, H. He, G. Li, W. Qian, G. Shen, D. Pommerenke, C. Ding, D. White, S. Scearce, and Y. Yang, "Designing a 3D printing based channel emulator," *in IEEE Int. Symp. EMC*, Rayleigh, NC, 2013, pp. 956-960.

[23] G. Li, G. Hess, R. Hoeckele, P. Jalbert, S. Davidson, V. Khilkevich, T. Van Doren, D. Pommerenke, and D. Beetner, "Measurement-based modeling and worst-case estimation of crosstalk inside an aircraft cable connector," *IEEE Trans. EMC*, vol. 57, no. 4, pp. 827-835, Aug. 2015.

SECTION

2. CONCLUSIONS

In the first paper, based on an electric field resonator cascaded with quarter-wave transformers, a resonant electric field probe was designed with higher sensitivity than a broadband probe. The short-ended stub (inductor) and open-ended stub (capacitor) can be tuned to achieve the desired resonant frequency for the resonator. The cascaded transformer converted the high loading impedance of the resonator to the input impedance of the measurement instruments for maximum power transfer at the resonance frequency. The transmission coefficient $|S_{21}|$ from a matched microstrip trace to the probe was used as the criteria to compare the resonant and broadband probes because power was transferred maximally when $|S_{21}|$ reached its peak. The measured $|S_{21}|$ of the resonant probe was 6.6 dB higher than that of the broadband probe at the resonant frequency of 1.577 GHz. The established methodology can be used to design resonant probes with high sensitivity at different resonant frequencies.

In the second paper, an equivalent SPICE model was developed to estimate the radiated emissions from partially shielded cables above a metal plate in component level tests, like those used for CISPR 25, MIL-STD 461, and DO-160. The dominant emissions result from currents in "ground" connections between the cables and the metal return plane for these setups. The currents in the ground connections can be predicted by modeling the cables above the ground plane as transmission lines and by considering the "ground" connections as inductors in series with radiation resistors. The fields from these currents can be approximated using infinitesimal dipoles. Applying the antenna factor of a biconial antenna to the fields gives the observed voltages. Comparisons between predicted and full-wave simulated/measured results demonstrate that this model is able to predict radiated emissions from 60 MHz up to 1 GHz. While the model was developed to predict emissions from shielded wires, it could also be applied to scenarios where the signal wires are unshielded. In that case, the source in Fig. 4 would be placed at the DUT (location x_1) and the entire length of cable from the DUT to load would be treated as a single transmission line. As a SPICE model, it is easy to integrate this model for

emissions with existing models of the component circuitry. The models can be applied without the need for sophisticated software or development of sophisticated numerical models. Equally important, since the models are simple, they help provide intuition as to the causes for radiated emissions problem and how they might be fixed.

In the third paper, an experimental methodology based on VNA measurements was developed in order to determine the coupling parameters within a cable bundle, and the characteristic impedance and effective dielectric constant of the wires. To predict the single-ended and differential crosstalk between the wires, an equivalent circuit model was created. The model was then validated against actual measurement results. A closed-form expression for estimating the worst-case crosstalk in the cable bundle, when the coupling mainly occurs inside the connector shell, was also derived and evaluated. The closed-form expression is shown to be reasonably accurate as maximum crosstalk estimates are generally within 6 dB of the peak crosstalk measured from this cable bundle. These results indicate this measurement-based method can be effective for analyzing complex aircraft cable assemblies and connectors without requiring extensive knowledge of the assembly procedure.

VITA

Guanghua Li was born in Sichuan Province, P. R. China, 1985. He received the Bachelor of Science degree in Electronic Information Technology (2008) and the Master of Science degree in Radio Physics (2011) from Sichuan University, Chengdu, P. R. China. He started his Ph.D. program in Electrical Engineering in 2011 in the Electrical and Computer Engineering Department at Missouri University of Science and Technology. He has also worked as a fall intern at Apple EMC Group for fall of 2015. He received his Ph.D. degree in Electrical Engineering in May 2016 from Missouri University of Science and Technology.